Dynamic Fluence Field Modulation for Low-Dose CT Using Multiple Aperture Devices

by

Andrew W. Mao

A dissertation submitted to The Johns Hopkins University

in conformity with the requirements for the degree of

Master of Science in Engineering

Baltimore, Maryland

May, 2018

Abstract

X-ray Computed Tomography (CT) is a major imaging modality used in a wide variety of clinical cases in modern medicine, but has raised public concerns over increasing population radiation exposure. While traditional dose-saving solutions, such as the bowtie filter, have been in use for several decades, researchers have faced significant hurdles in achieving dynamic fluence-field modulation (FFM), or generalized control over the x-ray fluence used in a CT examination. Multiple aperture device (MAD) based filtering has emerged as a promising hardware solution to realize FFM in a compact form factor that facilitates realistic integration into clinical CT scanners. MAD-based FFM offers significant dose reduction potential, but faces a unique set of challenges that must be overcome to confer meaningful clinical advantages over the traditional bowtie. We demonstrate with a newly developed processing pipeline that MADs can be used to generate clinically useful diagnostic images, and that MAD-based imaging can substantially benefit clinical workflow in challenging clinical scenarios like patient miscentering.

Thesis Committee

Primary Readers

J. Webster Stayman, Ph.D. (Primary Advisor)
Assistant Professor
Department of Biomedical Engineering
Johns Hopkins University

Wojciech B. Zbijewski, Ph.D.
Assistant Professor
Department of Biomedical Engineering
Johns Hopkins University

Katsuyuki Taguchi, Ph.D.
Associate Professor
Department of Radiology and Radiological Science
Johns Hopkins University

Acknowledgments

This dissertation represents my work in the Advanced Imaging Algorithms & Instrumentation Lab (AIAI) Lab for the past year and a half, but it is really the culmination of my five year journey in Biomedical Engineering at Johns Hopkins University. When I started here in the Fall of 2013, I had no idea what I was really interested in. It took me a couple of years of wandering around and exploring different avenues to find the AIAI Lab, but fortunately in my junior year I came to enroll in Prof. Jerry Prince's Medical Imaging Systems and Prof. J. Webster Stayman's Imaging Instrumentation course, where I was introduced to the wonderful world of medical imaging. Prof. Stayman's class was one of the most intensive classes I have ever taken, but also the most fun. I remember the sheer excitement I had when my group was able to reconstruct transmission images using a simple optical bench setup, and then emission images from our course project with fluorescent dye. It was one of the few moments in my BME career that I was really awestruck by what I was learning in class. Not too long thereafter, I made the best decision of my academic career to join the AIAI lab.

I want to express my deepest gratitude to Prof. Stayman for taking me on as his Master's student and supervising this work. He is an incredibly cheerful

and dedicated mentor who works hard to create an open and nurturing lab environment for his students. Prof. Stayman has always been available to offer support, encourage me when experiments were not working and provide clear scientific guidance which has helped shaped my scientific thinking and communication. He is a committed educator who sincerely and genuinely cares about his students. I would not be where I am today with his support, and I am very fortunate to have had him as an advisor.

I want to thank the other members of my thesis committee, Dr. Wojciech Zbijewski and Dr. Katsuyuki Taguchi, for their guidance and for reading my dissertation. I would also like to thank Dr. Jeffrey Siewerdsen for teaching me a lot of what I know about x-ray CT imaging and his time, support and feedback on my research. I greatly appreciate our funding from the NIH through grant U01-EB018758 and support from our U01 collaborators, including Dr. Satomi Kawamoto (Radiology) and Mr. Reuven Levinson (Philips). Thanks to all those in the AIAI Lab for their camaraderie, including Dr. Grace Gang, Dr. Hao Zhang, Steve Tilley, Wenying Wang, Gabriela Rodal, Lorenz Hehn, and Nischita Kaza; as well as the I-STAR Lab, including Dr. Alejandro Sisniega, Dr. Tharindu de Silva, Dr. Michael Brehler, Qian Cao, Niral Sheth, Michael Ketcha, Pengwei Wu, Runze Han, Thomas Yi, Michael Mow, Dr. Ali Uneri, Dr. Andrew Davis and Dr. Dong Zeng. Special thanks must go to Sam Bourne for making my transition to and time in the MSE program extremely smooth. I am very grateful to my friends outside the lab, with whom I have shared many memories of Baltimore I will cherish for a long time. Finally, I want to dedicate this thesis to my family for their never-ending love and support.

Table of Contents

List of Tables

List of Figures

Chapter 1

Introduction

1.1 X-ray Imaging and Computed Tomography

X-rays were first discovered by Wilhelm Roentgen in 1895, when he first produced a radiographic image of his wife's hand. This was a seminal discovery for which Roentgen was awarded the first Nobel Prize in Physics in 1901 and credited for founding the field of modern diagnostic radiology. In the century following Roentgen's discovery, researchers have uncovered a wide range of clinical applications for x-rays, which form the core of many medical imaging modalities including projection radiography, computed tomography, mammography, and fluoroscopic imaging, among many more. X-rays are now used to image the anatomy of all kinds of tissues and organs in the human body, including the heart, lungs, brain, gastrointestinal system and the musculoskeletal system.

This section presents a basic introduction to x-ray imaging physics and computed tomography. This material is based largely on the books Prince and Links (2015) and Bushberg et al. (2012), which provide more comprehensive

details and background on the topics covered here.

1.1.1 X-ray Imaging Physics

X-rays are a form of electromagnetic (EM) radiation, with energies in the diagnostic range typically between 10-150 keV. X-rays are formed when the kinetic energy of electrons is converted into electromagnetic radiation upon interaction with the target material. In the x-ray tube, the cathode is the source from which electrons accelerate to collide with the anode, which has a positive potential with respect to the cathode. A focusing cup is commonly employed to focus the electrons to a specific location on the anode, which is referred to as the focal spot.

Electrons colliding with the anode material – usually tungsten – undergo two main interactions which comprise the emitted x-ray spectrum. The first occurs when the electron is decelerated by positive attraction to the nucleus, consequently losing energy in the form of bremsstrahlung radiation. The intensity of this radiation is dependent on the incident energy of the electron and the atomic number of the atom. The second, termed characteristic radiation, occurs when the electron collides with a K-shell electron, thus ionizing the atom. This temporary vacancy is filled by an electron from the L, M, or N shells, which due to an increase in binding energy at the K-shell loses energy in the form of an x-ray photon, called characteristic radiation. The energy of the x-ray is therefore equal to the difference in binding energy between the shells.

X-rays experience four main types of interactions with matter. In the

diagnostic energy range, these interactions are predominantly photoelectric absorption and Compton scatter. Photoelectric absorption occurs when an incident x-ray ejects a K-shell electron, imparting all of its energy to the ejected electron. The probability of the photoelectric interaction is proportional to $(\frac{Z}{E})^3$, where Z is the atomic number and E is the energy of the photon. In Compton scatter, the incident photon ejects a valence electron, losing some of its energy to the ejected electron and also changing its direction. The energy of the scattered photon is dependent on this scattering angle.

The linear attenuation coefficient, μ, the tissue property measured in x-ray imaging, can be defined as the probability of photon interaction per unit length of a material. The relationship between the incident x-ray intensity (I_0) and transmitted intensity as a function of the linear attenuation coefficient is described by the Beer-Lambert Law,

$$I(E) = I_0(E)e^{-\int_0^L \mu(s;E)ds} \tag{1.1}$$

where E is the photon energy and L is the path length through the material. The exponential term in (1.1) is referred to as the transmissivity of the object.

X-rays transmitted through the patient are detected and measured using a variety of detection mechanisms. In digital radiography and in modern CT systems, this is commonly done via an indirect mechanism involving a scintillator to convert x-ray photons into optical light combined with a photodiode. In direct detection systems, x-rays are converted directly into electrical current, e.g., by use of a gas-filled ionization chamber.

1.1.2 Computed Tomography

X-ray Computed Tomography, or simply CT, is the extension of x-ray transmission imaging to producing cross-sectional images of the body, as opposed to simply projection images. CT was invented in the 1972 by Godfrey Hounsfield and Allan Cormack, who jointly shared the Nobel Prize in Physiology or Medicine in 1979. The first CT scanner built by Hounsfield required several hours to acquire data in the parallel beam geometry and several days to reconstruct a relatively coarse image. Since these first tomographic images produced in the 1970s, CT scanners have undergone many generations of technical development to now being capable of producing much higher quality images in fractions of a second. Along the way, key developments in the form of fan-beam acquisition, helical scanning, and multidetector CT have all enabled significant reductions in scan time and subsequently increased the utilization of CT in medicine. CT is now a major front-line imaging modality in modern medicine and is used for all kinds of clinical studies including the head, thorax, abdomen, and the musculoskeletal system. Recent estimates have placed the number of CT scans performed annually at 71 million in 2017 in the United States alone (IMV, 2017).

The fundamental theory underlying computed tomography is the projection-slice theorem, which states that the Fourier transform of a single 1D projection of the object acquired at rotation angle θ is equal to the radial slice in the 2D Fourier transform of the object at angle θ. If $F(u,v) = \mathcal{F}_{2D}\{f(x,y)\}$ is the

Fourier transform of the object, the Projection-Slice theorem states that

$$F(\rho,\theta) = \mathcal{F}_{1D}\{l(u,\theta)\} = P(\rho,\theta) \tag{1.2}$$

where u is the horizontal positional index on the detector, P is the Fourier transform of the line-integral (projection) data l and ρ,θ are the polar coordinates in the Fourier domain.

The projection-slice theorem consequently gives rise to the analytical reconstruction algorithm called Filtered Backprojection. In the parallel-beam case, the object image $f(x,y)$ is

$$f(x,y) = \int_0^{\pi} \left[\int_{-\infty}^{\infty} P(\rho,\theta)|\rho| e^{j2\pi\rho u} d\rho \right]_{u=x\cos\theta+y\sin\theta} d\theta \tag{1.3}$$

where $|\rho|$ is a "ramp" filter in the frequency domain. Because radial sampling leads to sparser sampling at high frequencies, the ramp filter compensates for the "blur" associated with the backprojection operation by re-weighting the frequency data. To avoid amplifying high frequency noise, the ramp filter is commonly implemented with a cutoff at or below the Nyquist sampling frequency. The interpretation of FBP reconstruction is therefore a filtering in the frequency domain by the ramp filter, followed by backprojection over the line $x\cos\theta + y\sin\theta$ and summation over all rotation angles. Equation (1.3) can easily be extended to the fan-beam geometry with the use of coordinate transforms and the application of appropriate weighting terms to account for the geometric differences in sampling.

In recent years, cone-beam CT has emerged as a useful imaging modality in operating rooms and interventional suites. Cone-beam CT systems generally

utilize a flat-panel detector with many more detector rows along the vertical (v) direction than traditional CT systems, which have very small cone angles. Commonly constructed in the form of a “C-arm," these systems have a smaller physical footprint than traditional CT scanners and are more flexible in the way they can be positioned around the patient, though they exhibit slower rotation speeds and artifacts associated with cone-beam data acquisition. FBP can also similarly be extended to the cone-beam case and is known as the Feldkamp-Davis-Kress algorithm, or FDK algorithm (Feldkamp, Davis, and Kress, 1984). FDK is the primary reconstruction algorithm used for the work presented in this thesis, as the test-bench system used in the investigations was based on a flat-panel setup and a cone-beam geometry.

While not the focus of this thesis, much attention in recent years has also been given to model-based iterative reconstruction methods (MBIR). MBIR can outperform the analytical FBP algorithm in image quality by incorporating image priors and noise models for the measured data, at the cost of computation time.

1.2 Low-dose CT

1.2.1 Clinical Motivation

Increased use of diagnostic CT in modern medicine over the past few decades have raised concerns over population radiation exposure levels. To quantify the radiation dose in CT, researchers have used a variety of metrics. The volume CT dose index (CTDI_{vol}), reported in milliGray (mGy), is the dose to a body volume measured using a standardized CT dosimetry (CTDI) phantom.

The absorbed dose, also measured in mGy, is the dose deposited in the body, usually with a consideration of the specific patient's size. The effective dose, measured in milliSieverts (mSv), is similar to absorbed dose but additionally takes into account the varying radiation sensitivities of different organs and tissues in the body.

The effective dose measure may allow a standardized comparison of the amount of ionizing radiation across a variety of CT examinations and exposure levels. Table 1.1 summarizes the effective dose for a variety of medical imaging exams involving ionizing radiation (McCollough et al., 2015). Though

Table 1.1: Effective dose statistics by type of examination.

Exam	Effective dose (mSv)
Chest radiograph	0.02
Mammogram	0.4
Head CT	2
Chest CT	7
Abdominal CT	8
Coronary CT Angiogram	16
Annual Naturally Occurring Background Radiation	3

the effective dose values for these exams are below the 100 mSv threshold for radiation levels typically associated with increased cancer risk (Preston et al., 2007), the topic of cancer risk from CT scans is highly controversial. It is certainly true that exposures can accumulate over time if the patient is to be subject to multiple exams or longitudinal imaging studies. Additionally, as most CT examinations have effective dose levels above the annual "background" radiation levels (3 mSv), there has been significant public interest in

reducing dose levels from routine CT studies to a fraction of this level.

Recent efforts have strived to reduce radiation exposure levels and have set "sub-mSv CT" as a general target for diagnostic studies. As described in (McCollough et al., 2012), the majority of research in this area can be categorized as 1) innovations in detector technology, e.g. by reducing electronic noise, improving scintillator efficiency or by developing photon-counting detectors (PCDs); 2) optimizing image acquisition protocols to utilize x-ray dose in a more efficient manner; or 3) sophisticated reconstruction methods (like MBIR) to produce images of greater image quality than traditional reconstruction techniques at the same dose level, consequently reducing the necessary exposure to achieve the same image quality. The work in this thesis primarily focuses on methods to optimize image acquisition methods in CT, which is further explored in the following sections.

1.2.2 Patient-Specific Image Acquisition

Clinical CT scanners have traditionally been somewhat limited in their ability to customize their data acquisitions to the patient. This can result in CT studies that are ordered with a “one-size fits all” mentality. Optimal data acquisitions can vary significantly from patient to patient based on the anatomical site or the imaging task, and there can be significant radiation dose consequences of not performing a customized acquisition—essentially delivering more radiation than is needed to accomplish a medical diagnosis. Recognizing the importance of patient-specific imaging protocols, campaigns like Image Gently and Image Wisely have recommended the use of exposure charts based

on patient size (Goske et al., 2008; Brink and Amis, 2010).

Automatic exposure control (AEC) is one technique for adaptive and patient-specific imaging that is commercially available and commonly used. AEC is based on the observation that the attenuation of the x-ray beam varies with rotation angle because the cross section of the human body differs significantly from a circular shape. As a result, quantum noise also varies widely, leading to inhomogeneous noise patterns in the reconstructed image. AEC may be used to control noise by adapting the x-ray intensity to the projection-dependent attenuation, e.g. by dynamically modulating the tube current. Work by Gies et al. (1999) helped formulate the general equation

$$I_0(u,\theta) = \frac{\exp \alpha l(u,\theta)}{\sum_\theta \exp \alpha l(u,\theta)} I_0^{tot} \tag{1.4}$$

where I_0^{tot} is the total exposure constraint and $I_0(u,\theta)$ is the emitted x-ray intensity needed for the measurement denoted by u, the positional index across the detector, and θ, the view angle. α is a scalar that controls the amplitude of modulation, where there are three strategies of particular interest: $\alpha = 0$, the unmodulated case; $\alpha = 0.5$, the strategy that produces the minimum mean variance in the image reconstructed by FBP; and $\alpha = 1.0$, the strategy producing the most uniform distribution of noise in the reconstruction.

In practice, the beam modulation described by (1.4) cannot be achieved by tube-current modulation (TCM) alone, as TCM cannot create the spatially varying (with u) x-ray intensity to match the attenuation profile of the human body. To achieve this, CT systems commonly rely on beam-shaping, or bowtie filters. Bowtie filters are typically made from a low-Z material like aluminum

or Teflon and shape the x-ray beam spatially through selective attenuation to decrease the fluence incident to the patient for measurements expected to have a lower overall attenuation. These filters are often also designed to homogenize noise by promoting a uniform detector signal, commonly by assuming a homogeneous, circular object of a specific size in the field of view (Wunderlich and Noo, 2007; Toth et al., 2005). Commercial CT systems are often equipped with a few choices of bowtie filters corresponding to “large,” “medium," or “small” patient sizes, for example.

Researchers have sought to optimize many other aspects of image acquisition, including the x-ray spectra through automatic kV selection (Yu et al., 2010), greatly reducing the peripheral radiation dose for volume-of-interest imaging (Kolditz, Kyriakou, and Kalender, 2010), and using dynamic z-axis beam collimation in helical CT (Deak et al., 2009). Work by Szczykutowicz et al. (2015) has attempted to consolidate developments in patient and task-specific acquisition by developing optimal clinical CT protocols for a wide range of imaging scenarios. This comprehensive list of protocols includes the clinical indications for all kinds of CT imaging, the type and and amount of contrast agent to use, and the best scan and reconstruction parameters to use for certain tissue types, among other information.

1.2.3 Fluence Field Modulation

One major drawback to the design of traditional bowtie filters used in CT scanners is that patients are not radially symmetric—i.e., the patient’s cross-section is closer to an ellipse than a circle. Additionally, patient miscentering

can cause severe penalties in dose and image quality (Toth, Ge, and Daly, 2007). To better accommodate patient width variability and miscentering problems, there has been significant research interest in achieving dynamic fluence field modulation (FFM). Such a FFM capability would permit optimized fluence patterns based on the patient's size, position in the scanner, and imaging task. Dynamic FFM can be thought of as a generalization of AEC wherein one has the ability to modulate the spatial distribution of x-ray flux, in addition to a frame-to-frame/angular exposure variation.

There has been much theoretical work regarding how to design the fluence modulation pattern that should be delivered to the patient. Harpen (1999) analytically derived the FFM strategy that yields the minimum mean variance in the FBP reconstructed image. Bartolac et al. (2011) proposed a method to design the FFM strategy to meet a prescribed image quality objective under a radiation exposure constraint. Hsieh and Pelc (2014) developed FFM algorithms to minimize the mean variance, weighted mean variance, and peak variance in FBP reconstruction. Gang, Siewerdsen, and Stayman (2017) showed the optimal FFM design strategy to maximize human observer performance for a specific imaging task and MBIR.

Achieving practical dynamic FFM, however, requires the development and integration of new beam modulation hardware into the CT gantry. To realize "dynamic bowties," researchers have proposed a number of methods. Many approaches seek to modulate the spatial beam profile by moving attenuating bowtie elements in and out of the field of view. Dynamic bowtie methods include: 1) Double wedge systems (Toth, Tkaczyk, and Hsieh, 2007), which

involve two split halves of a bowtie that can be translated laterally, thus adapting the width of the x-ray beam; 2) piecewise linear filters (Hsieh and Pelc, 2013; Hsieh et al., 2016) constructed from a series of wedges that can be individually actuated within the beam path to achieve variable attenuation; 3) Fluid-filled bowties (Shunhavanich, Hsieh, and Pelc, 2015; Szczykutowicz and Hermus, 2015) that modify the attenuation path by using a two dimensional array of elements that can be filled or unfilled with attenuating fluids; And 4) a related strategy based on digital beam attenuators (Szczykutowicz and Mistretta, 2013; Szczykutowicz and Mistretta, 2014) achieves beam modulation by combining several exposures with an essentially binary filter at different locations.

1.2.4 Multiple Aperture Devices

An emerging technology for dynamic beam filtration based on multiple aperture devices (MADs) (Stayman et al., 2016; Mathews et al., 2016) can shape the x-ray beam while maintaining a compact profile (i.e., the MAD filters are $\sim$2 mm thick). This is important since modern CT gantries allow little room for additional hardware in front of the x-ray tube, and finding compact beam filtration solutions and actuation hardware within the limited space of a clinical CT scanner is a challenge.

MAD filters are essentially binary and block or pass x-rays using small slit-shaped apertures in a high-density material (e.g., tungsten), as seen in Figure 1.1. MADs operate under the following principle: wider slits permit higher local fluence while thinner slits restrict local fluence. Moreover, the local size

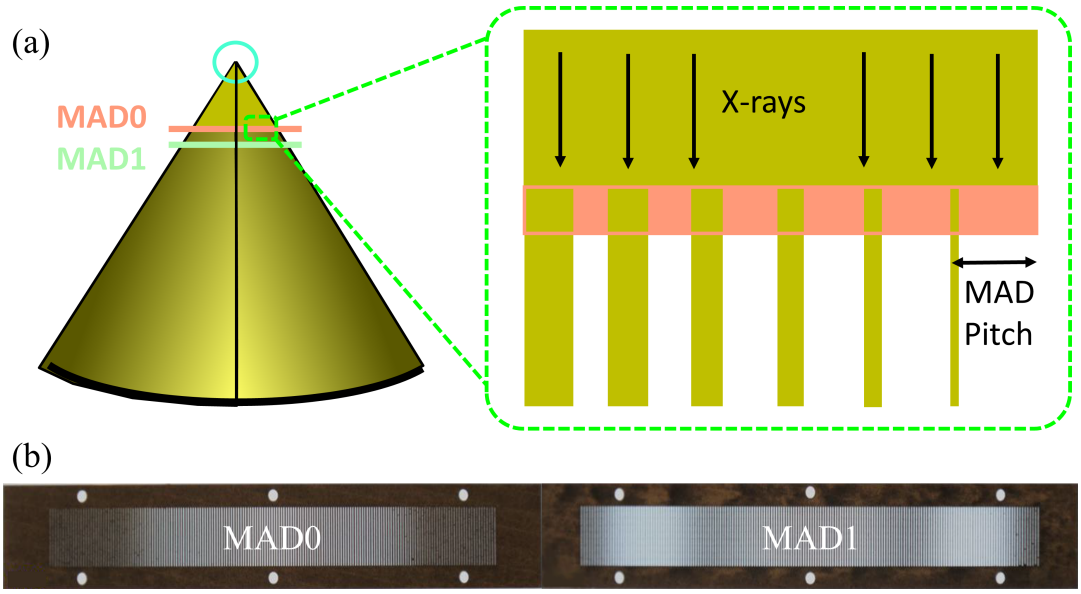

Figure 1.1: Multiple aperture devices. (a) Placement of the MADs in the beam path and a close-up view of the periodic grating structure. (b) Optical image of MAD0 and MAD1.

and spacing of the tungsten slits can be optimized for two MADs placed in series in front of the x-ray beam to achieve a wide range of modulation patterns. In essence, the two binary MAD filters create low frequency Moiré patterns of varying shapes and widths which can be varied via relative displacement of one MAD (MAD1) with respect to the other (MAD0). These modulation patterns become cyclic for translations greater than one MAD “period," which is equal to the distance between neighboring apertures (labeled the “pitch" in Figure 1.1a). Similarly, the center of the beam profile may be shifted by changing the absolute positioning of both filters simultaneously. Since the slits are small relative to the resolution limiting elements of the system (e.g. the x-ray focal spot), the induced modulation patterns can be relatively smooth even though the filters are binary. A dual-MAD based filtration scheme offers both centering and width control of the beam with small (mm scale) linear

actuation.

Because of their unique design, imaging with MADs has an additional set of challenges that need to be overcome before they can be clinically useful. This is explored in more detail in the proceeding chapters.

1.3 Thesis Overview and Outline

Thesis Statement: Dynamic fluence-field modulation based on multiple aperture devices can be used to reconstruct diagnostic quality CT images, optimize dose utilization and improve uniformity of image properties in challenging clinical scenarios such as patient miscentering.

Chapter 2 presents the initial work towards developing a modified pipeline to generate artifact-free image reconstructions in MAD imaging. Chapter 3 describes the design of dynamic FFM for miscentered patients and results of experimental studies conducted with physical phantoms. Chapter 4 summarizes the work, discusses the remaining challenges and future directions for the MAD-based filtering concept.

References

Prince, Jerry L. and Jonathan M. Links (2015). *Medical Imaging Signals and Systems*. Upper Saddle River, NJ: Pearson.

Bushberg, Jerrold T, Anthony J Seibert, Edwin M Leidholdt, and John M Boone (2012). *The essential physics of medical imaging*. Philadelphia, PA: Lippincott Williams & Wilkins.

IMV (2017). *IMV 2017 CT Market Outlook Report*. URL: https://www.imvinfo.com/index.aspx?sec=ct&sub=def (visited on 04/11/2018).

Feldkamp, L. A., L. C. Davis, and J. W. Kress (1984). "Practical cone-beam algorithm". In: *J. Opt. Soc. Am. A* 1.6, pp. 612–619. DOI: 10.1364/JOSAA.1.000612.

McCollough, Cynthia H., Jerrold T. Bushberg, Joel G. Fletcher, and Laurence J. Eckel (2015). "Answers to Common Questions About the Use and Safety of CT Scans". In: *Mayo Clinic Proceedings* 90.10, pp. 1380–1392. DOI: 10.1016/j.mayocp.2015.07.011.

Preston, D. L., E. Ron, S. Tokuoka, S. Funamoto, N. Nishi, M. Soda, K. Mabuchi, and K. Kodama (2007). "Solid cancer incidence in atomic bomb survivors: 1958-1998". In: *Radiat. Res.* 168.1, pp. 1–64. DOI: 10.1667/RR0763.1.

McCollough, C. H., G. H. Chen, W. Kalender, S. Leng, E. Samei, K. Taguchi, G. Wang, L. Yu, and R. I. Pettigrew (2012). "Achieving Routine Submillisievert CT Scanning: Report from the Summit on Management of Radiation Dose in CT". In: *Radiology* 264.2, pp. 567–580. DOI: 10.1148/radiol.12112265.

Goske, M. J., K. E. Applegate, J. Boylan, P. F. Butler, M. J. Callahan, B. D. Coley, S. Farley, D. P. Frush, M. Hernanz-Schulman, D. Jaramillo, N. D. Johnson, S. C. Kaste, G. Morrison, K. J. Strauss, and N. Tuggle (2008). "The Image Gently campaign: working together to change practice". In: *AJR Am J Roentgenol* 190.2, pp. 273–274. DOI: 10.2214/AJR.07.3526.

Brink, J. A. and E. S. Amis (2010). "Image Wisely: a campaign to increase awareness about adult radiation protection". In: *Radiology* 257.3, pp. 601–602. DOI: 10.1148/radiol.10101335.

Gies, Michael, Willi A. Kalender, Heiko Wolf, Christoph Suess, and Mark T. Madsen (1999). "Dose reduction in CT by anatomically adapted tube current modulation. I. Simulation studies". In: *Medical Physics* 26.11, pp. 2235–2247. DOI: 10.1118/1.598779.

Wunderlich, Adam and Frédéric Noo (2007). "Achieving uniform noise in direct fan-beam CT reconstruction through bowtie filter design". In: *IEEE Nuclear Science Symposium Conference Record* 6, pp. 4379–4382. DOI: 10.1109/NSSMIC.2007.4437083.

Toth, T L, E Cesmeli, A Ikhlef, and T Horiuchi (2005). "Image quality and dose optimization using novel x-ray source filters tailored to patient size". In: *Progress in Biomedical Optics and Imaging - Proceedings of SPIE* 5745.I, pp. 283–291. DOI: 10.1117/12.595465.

Yu, Lifeng, Hua Li, Joel G. Fletcher, and Cynthia H. McCollough (2010). "Automatic selection of tube potential for radiation dose reduction in CT: A general strategy". In: *Medical Physics* 37.1, pp. 234–243. DOI: 10.1118/1.3264614.

Kolditz, D., Y. Kyriakou, and W. A. Kalender (2010). "Volume-of-interest (VOI) imaging in C-arm flat-detector CT for high image quality at reduced dose". In: *Med Phys* 37.6, pp. 2719–2730. DOI: 10.1118/1.3427641.

Deak, P. D., O. Langner, M. Lell, and W. A. Kalender (2009). "Effects of adaptive section collimation on patient radiation dose in multisection spiral CT". In: *Radiology* 252.1, pp. 140–147. DOI: 10.1148/radiol.2522081845.

Szczykutowicz, Timothy P., Robert K. Bour, Nicholas Rubert, Gary Wendt, Myron Pozniak, and Frank N. Ranallo (2015). "CT protocol management: Simplifying the process by using a master protocol concept". In: *Journal of Applied Clinical Medical Physics* 16.4, pp. 228–243. DOI: 10.1120/jacmp.v16i4.5412.

Toth, T., Z. Ge, and M. P. Daly (2007). "The influence of patient centering on CT dose and image noise". In: *Medical Physics* 34, pp. 3093–3101. DOI: 10.1118/1.2748113.

Harpen, Michael D (1999). "A simple theorem relating noise and patient dose in computed tomography." In: *Medical physics* 26.11, pp. 2231–4. DOI: 10.1118/1.598778.

Bartolac, Steven, Sean Graham, Jeff Siewerdsen, and David Jaffray (2011). "Fluence field optimization for noise and dose objectives in CT". In: *Medical Physics* 38.S1, S2–S17. DOI: 10.1118/1.3574885.

Hsieh, Scott S. and Norbert Joseph Pelc (2014). "Algorithms for optimizing CT fluence control". In: *Proceedings of SPIE* 9033, pp. 90330M1–6. DOI: 10.1117/12.2042542.

Gang, G J, J H Siewerdsen, and J W Stayman (2017). "Task-Driven Optimization of Fluence Field Regularization for Model-Based Iterative Reconstruction in Computed Tomography". In: *IEEE Transactions on Medical Imaging* 36.12, pp. 2424–2435.

Toth, Thomas L, J. Eric Tkaczyk, and Jiang Hsieh (2007). "Method and apparatus of radiographic imaging with an energy beam tailored for a subject to be scanned". In: US Patent 7,076,029.

Hsieh, Scott S. and Norbert J. Pelc (2013). "The feasibility of a piecewise-linear dynamic bowtie filter". In: *Medical Physics* 40.3, p. 031910. DOI: 10.1118/1.4789630.

Hsieh, Scott S, Mark V Peng, Christopher A May, Picha Shunhavanich, Dominik Fleischmann, and Norbert J Pelc (2016). "A prototype piecewise-linear dynamic attenuator". In: *Physics in Medicine and Biology* 61.13, pp. 4974–4988. DOI: 10.1088/0031-9155/61/13/4974.

Shunhavanich, Picha, Scott S. Hsieh, and Norbert J. Pelc (2015). "Fluid-filled dynamic bowtie filter: a feasibility study". In: *Proc. of SPIE Medical Imaging 2015: Physics of Medical Imaging* 9412, pp. 94121L1–8. DOI: 10.1117/12.2081673.

Szczykutowicz, Timothy P. and James Hermus (2015). "Fluid dynamic bowtie attenuators". In: *Proc. of SPIE Medical Imaging 2015: Physics of Medical Imaging* 9412, pp. 94120X1–7. DOI: 10.1117/12.2077618.

Szczykutowicz, Timothy P. and Charles A. Mistretta (2013). "Design of a digital beam attenuation system for computed tomography. Part I. System design and simulation framework". In: *Medical Physics* 40.2, p. 021905. DOI: 10.1118/1.4773880.

Szczykutowicz, T. P. and C. A. Mistretta (2014). "Experimental realization of fluence field modulated CT using digital beam attenuation". In: *Physics in Medicine and Biology* 59.5, pp. 1305–1326. DOI: 10.1088/0031-9155/59/5/1305.

Stayman, J. Webster, Aswin Mathews, Wojciech Zbijewski, Grace Gang, Jeffrey Siewerdsen, Satomi Kawamoto, Ira Blevis, and Reuven Levinson (2016). "Fluence-Field Modulated X-ray CT using Multiple Aperture Devices". In: *Proc. of SPIE Medical Imaging 2016: Physics of Medical Imaging* 9783, pp. 97830X1–6. DOI: 10.1117/12.2214358.

Mathews, A. J., S. Tilley, G. Gang, S. Kawamato, W. Zbijewski, J. H. Siewerdsen, R. Levinson, and J. W. Stayman (2016). "Design of dual multiple aperture devices for dynamical fluence field modulated CT". In: *Conf Proc Int Conf Image Form Xray Comput Tomogr* 4, pp. 29–32.

Chapter 2

MAD Reconstruction

2.1 Introduction

Multiple aperture devices (MADs) have the potential to realize dynamic FFM by offering greater control over the fluence field in terms of both beam width and centering. Initial work on the basic operating theory, design process, fabrication and integration of the MADs suggest that the MADs are compact and can realistically be integrated into clinical CT scanners (Stayman et al., 2016; Mathews et al., 2016).

Figure 2.1 demonstrates the intuitive advantage of MAD-based FFM in the case of a uniform elliptical PMMA phantom. The MAD FDK reconstruction exhibits more uniformity of noise throughout the image, whereas the reference image (obtained in scan without using any FFM) has significantly reduced noise at the edge of the object compared to the center. This results from the improved dose utilization in the dynamic bowtie case which is optimized for the elliptical object. However, the MAD reconstruction exhibits significant image artifacts in the form of rings that are superimposed on the true image,

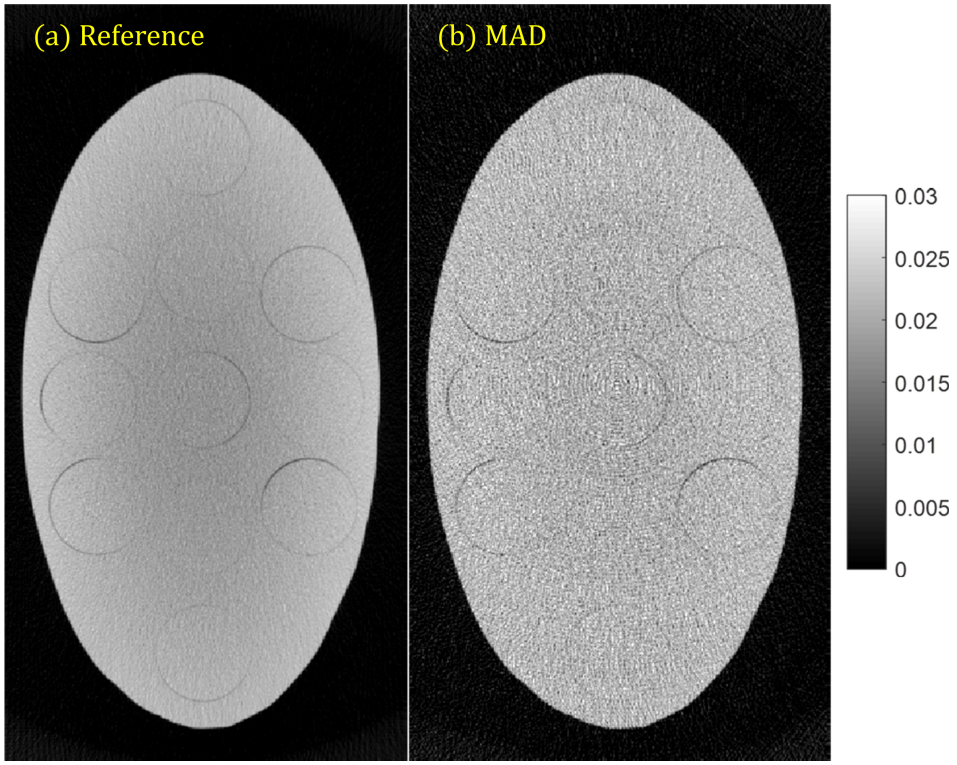

Figure 2.1: FDK reconstruction of elliptical phantom from (a) reference scan without beam filtering and (b) scan using MAD-based FFM. Ring artifacts are evident in the MAD case. Note that the dose is not matched between the two cases, because the baseline MAD transmissivity is below 50%.

as seen in Figure 2.1b.

A ring artifact arises from an error in the detected value of a single channel over an extended range of views. Generally, an error in an isolated view maps to a straight line in the backprojection process, creating a "streak." When the error at the same pixel persists over multiple views, the tail portions of the streak are canceled, but a ring is constructively generated (*Computed Tomography Principles, Design, Artifacts, and Recent Advances*). As a consequence of this constructive addition in the backprojection process, even if the individual channel error is small, the resultant ring artifact magnitude can be fairly large.

Hence, even though the noise level in Figure 2.1b is fairly high, the rings are still perceivable by the human observer.

In general, image artifacts can be defined as discrepancies in the image to the "true" attenuation coefficients of the object. While they are certainly undesirable, certain image artifacts (such as isolated streaks or partial volume effects) do not irretrievably degrade image quality, as radiologists are well-trained to read images in the presence of certain artifacts (*Computed Tomography Principles, Design, Artifacts, and Recent Advances*). However, radiologists can have difficulty reading through images with ring artifacts as they can obscure significant image content or even mimic certain pathologies. Consequently, the clinical utility of such images is significantly diminished.

Because the ring artifacts in Figure 2.1b occur at a regular radial frequency, it is unlikely that they arise from any individual pixel defects, which would also likely appear in the reference scan. Instead, it must be related to the high frequency grating structure of the MAD. This chapter presents work to characterize the source of the ring artifacts and proposes a correction scheme, which is primarily based on Gang et al. (2018 (accepted)[a]), Gang et al. (2018 (accepted)[b]), and Gang et al. (2018 (submitted)).

2.2 Blur Correction

The first hypothesized source of ring artifacts is related to the high frequency content in the MAD fluence patterns. As a result of the design, small deviations in these high frequency patterns between data acquisition y and the MAD transmissivity M can lead to small errors in "MAD gain correction,"

giving rise to ring artifacts (M is obtained simply by scanning the MAD without object and dividing by the air gain). To test this hypothesis, scans of the elliptical phantom were conducted by leaving approximately half of the vertical MAD extent (along the detector's v direction) "in air." The MAD fluence pattern was obtained by averaging detector rows in the MAD air region, presuming that the MAD pattern is uniform in the vertical direction. As seen in Figure 2.2a, there are significant mismatches in the MAD fluence profile in air between M and y. In addition to the difference in magnitude, as seen in Figure 2.2b, the high frequency content in y and M varies.

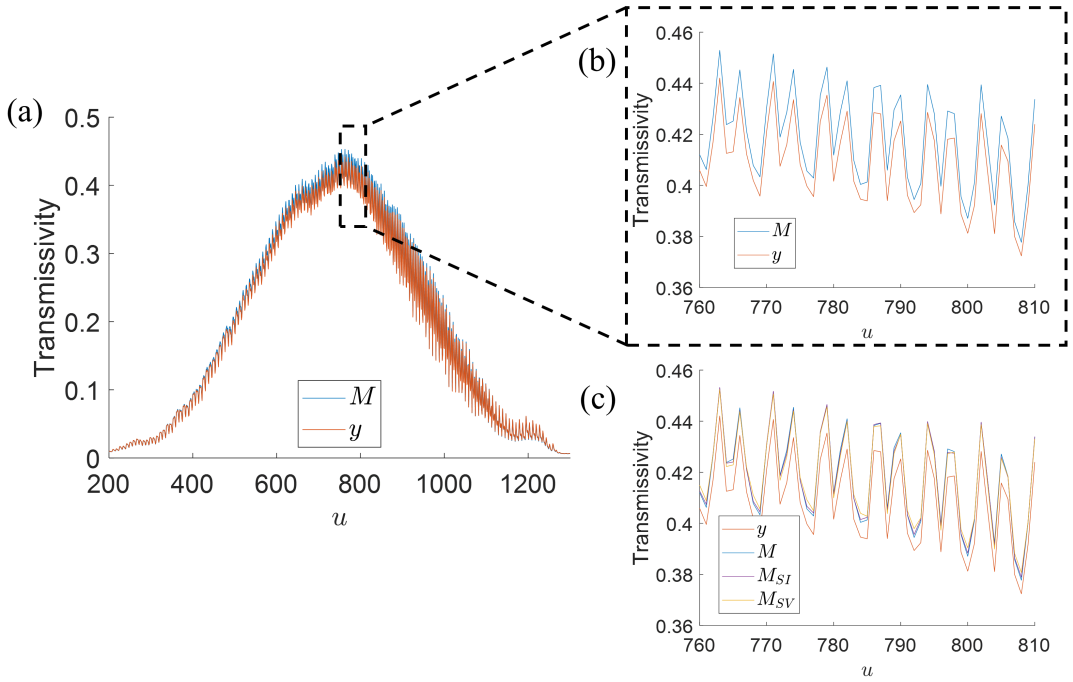

Figure 2.2: (a) Line profiles of the MAD fluence obtained by averaging rows of M and y. (b) Small portion of the projection illustrating the mismatch in high frequency content. (c) Corrected projection data using shift-invariant and shift-variant blur correction methods.

These high frequency deviations are also observed when the stationary MAD is simply imaged over an extended period of time. This led to the

hypothesis that these fluctuations arise due to focal spot effects; namely, changes in the focal spot size or position over time. If this is true, these focal spot effects can be modeled as a blur function in the detector plane along the u (horizontal) direction. Mathematically, this follows the measurement equation

$$\bar{Y}(u) = G(u)\,(B * M(u))\,e^{-l(u)} \tag{2.1}$$

where G is the gain term which encapsulates the emitted x-ray distribution from the tube and the x-ray detector sensitivity, M is the MAD transmissivity obtained from a previous scan, B is the blur kernel applied along the u direction and $*$ denotes the discrete convolution operation. We can divide out G to eliminate the detector sensitivity effects and since the line integral is zero in the air region a, we obtain

$$y^a(u) = \frac{Y^a(u)}{G^a(u)} = B * M^a(u) \tag{2.2}$$

B can thus be estimated by minimizing the mean squared error,

$$\arg\min_B \|B * M^a(u) - y^a(u)\|_2^2 \tag{2.3}$$

In this model, however, B also captures magnitude variations between M and y which could possibly arise from uncorrected x-ray scatter. To ensure B accounts only for focal spot effects, we modify (2.3) as

$$\begin{gathered}\arg\min_B \|B * \mathrm{dtr}\,\{M^a(u)\} - \mathrm{dtr}\,\{y^a(u)\}\|_2^2 \\ \text{subject to} \sum B = 1\end{gathered} \tag{2.4}$$

to incorporate the "detrending" operator, $\mathrm{dtr}\{\cdot\}$, which can simply be thought

of as a high-pass filter, and a constraint on the blur kernel to have a normalized integrated value.

While this formulation presumes that B is a shift-invariant operator, it is well-known that focal spot blur can be variable across the field of view due to obliquity effects. Therefore, it may be more appropriate to model a shift-variant blur that is variable with ray angle. This leads to two distinct models: the shift-invariant and shift-variant blurs we denote as B_{SI} and B_{SV} respectively. In the shift-invariant case, the simple relationship

$$M_{SI} = B_{SI} * M \tag{2.5}$$

to calculate the blur corrected MAD transmissivity holds.

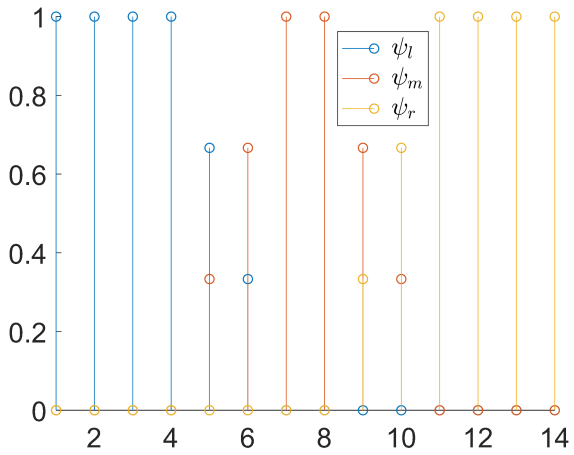

Figure 2.3: ψ_k weighting function for $L = 6$ and $l = 2$, where l denotes the left-most segment on the detector, r the right-most segment, and m any segment in between. The non-unity weights indicate the regions of overlapping segments.

Because the v extent of the MAD is small, we presume that the shift-variance in blur is primarily along the u direction of the detector. To model shift-variance, the u detector extent is divided into K horizontal segments of equal length L, and we estimate an individual blur B_k per segment $k \in$

$\{1, 2, \ldots, K\}$ according to

$$\hat{B}_k = \arg\min_B \|B * \mathrm{dtr}\{M_k^a\} - \mathrm{dtr}\{y_k^a\}\|_2^2 \quad \text{subject to} \sum B = 1 \tag{2.6}$$

where M_k and y_k denote the modified measurements that are zero outside the segment k. Each segment k may also have an overlapping region $l < L$, which can improve the modeling of shift-variant blur. This necessitates the use of a weighting function ψ that is unity within the segment and zero elsewhere, but performs the weighted average of the contributions from neighboring segments for each overlap region. An example ψ for a segment with $L = 6$ and overlap $l = 2$ is shown in Figure 2.3 for a detector of length 14.

From B^k, we now have the relationship

$$M_{SV} = \sum_{k=1}^{K} \psi_k \odot (B_k * M_k) \tag{2.7}$$

where $\odot$ denotes element-wise multiplication operation.

For MAD acquisitions, B can thus be estimated in the detector plane by using the MAD air region, which serves as a fiducial for the state of the focal spot for each projection view. In practice, blur estimation is again performed by averaging over the rows in a to decrease the noise in the projection. Figure 2.4 shows an example B_{SI} of width $w = 11$, which resembles a sinc function, and its evolution when imaging a static MAD scene for an extended period of time. The estimated blur kernel with respect to the prior "MAD gain" scan begins close to the delta function but exhibits increasingly negative sidelobes with increasing frame number, as seen in Figures 2.4c and 2.4d, which is

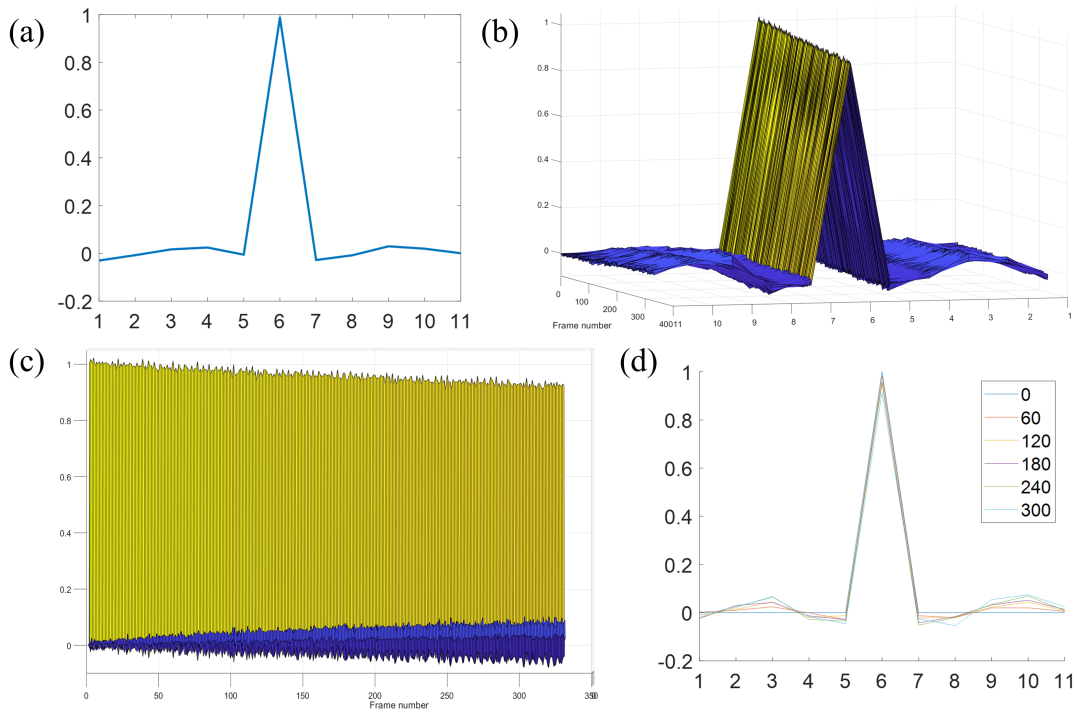

Figure 2.4: (a) Example of an estimated blur kernel B_{SI}. (b) Surface plot of B_{SI} over time for a static MAD scene with side-view in (c) and six evenly spaced time-points overlaid in (d).

consistent with the hypothesis of generally increasing blur over time.

The results of blur correction with both M_{SI} and M_{SV} for the elliptical PMMA phantom is summarized in Figure 2.5. The line profiles from the correction are shown in Figure 2.2c. Figure 2.5a shows the bar patterns that are evident in the air region in the uncorrected data, which are partially removed by shift-invariant blur correction (Figure 2.5c) and almost completely eliminated by shift-variant blur correction (Figure 2.5e). However, the line integral (log-scale) images show that the bar patterns in the object region remain after both correction strategies (Figures 2.5d and 2.5f).

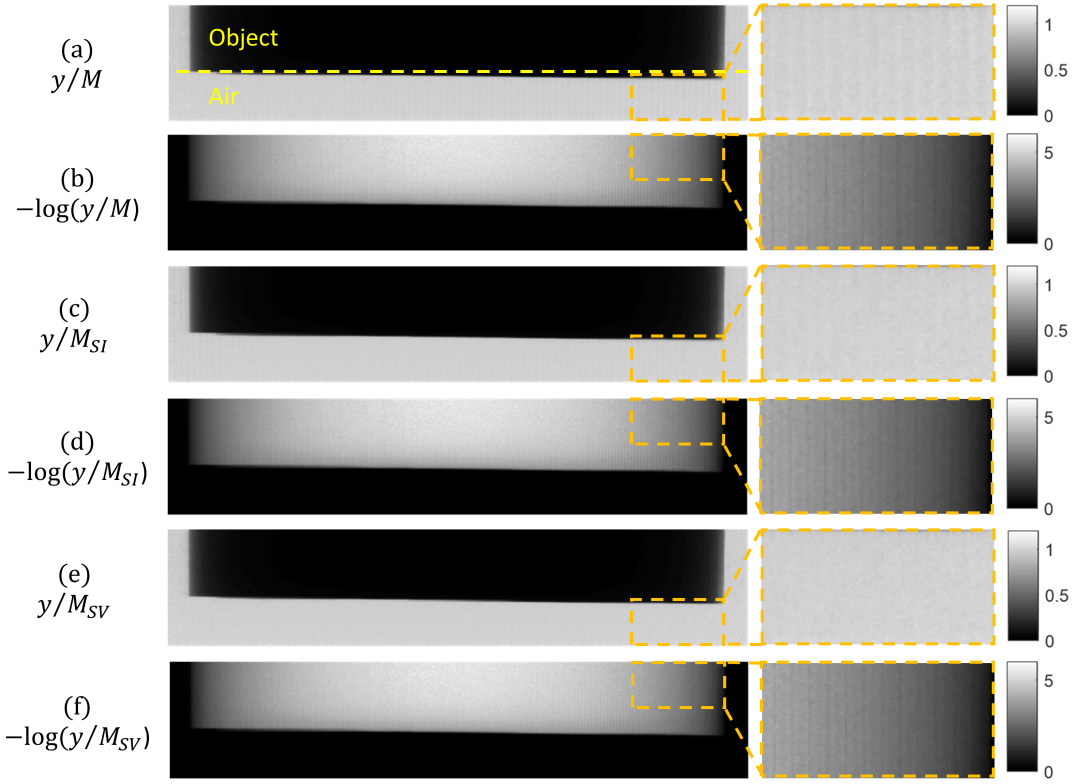

Figure 2.5: Comparison of blur correction results for the long-axis projection of an elliptical phantom on pre-log and log scales. (a-b) Uncorrected data; (c-d) shift-invariant blur corrected data; and (e-f) shift-variant blur corrected data. The object and air regions of the MAD are roughly divided by the yellow dashed line.

2.3 Spectral Correction

As the periodic high frequency bar patterns remain in the projection data in Figure 2.5f, there must be another effect that is not properly accounted for in the measurement model. Gang et al. (2018 (accepted)[b]) suggests that the binary transmission model through the MAD tungsten slits may not be entirely accurate. While the x-rays are assumed to be completely stopped by tungsten, incomplete blockage can cause lower energy x-rays to be preferentially attenuated, resulting in a beam hardening effect that changes the effective mean energy of the beam. This would create a lower

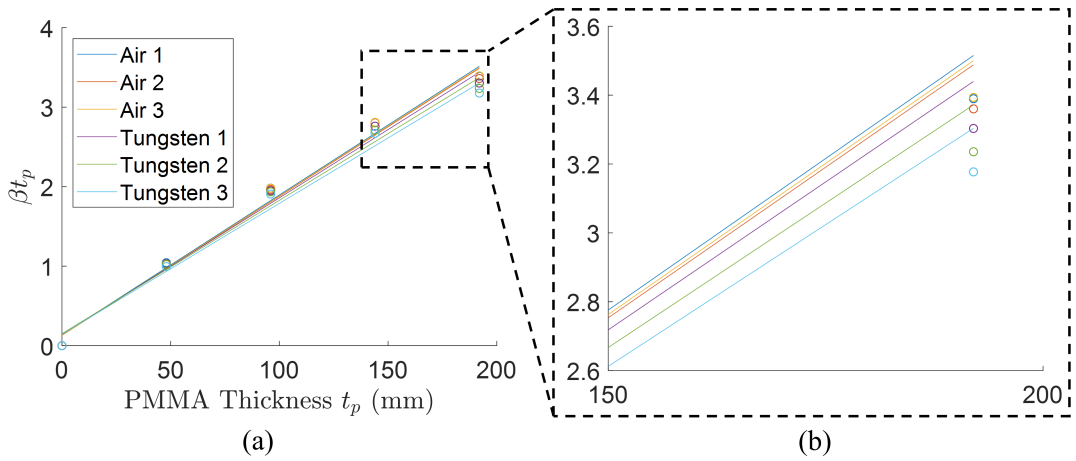

Figure 2.6: (a) Log-domain PMMA calibration data and estimated slopes for three separate points “in air" and “in tungsten" with increasing local slit size from 1 to 3. (b) Differences in slope are related to the tungsten slit size. Note however that the local slit size is not quantified here and is simply identified based on inverse proportionality to magnitude of the local x-ray fluence.

line integral value than expected at each MAD slit position, and result in the high frequencies observed in the projection data. The magnitude of these high frequency deviations depends on the degree of beam hardening, which in turn depends on the location and size of the local tungsten blockers.

If this is a spectral effect, a spectral “transfer function” of the MAD can be estimated from a prior MAD scan (conducted at the same actuation position) using a homogeneous (non-rotating) object. In this work, this calibration is performed using homogeneous slabs of PMMA which cover the full length of the detector. Acquisitions are repeated for various thicknesses of the PMMA slabs with the same exposure technique, from which the line integral measurements are used to estimate the linear slope in the log-domain by least-squares regression. Figure 2.6 shows the estimated slopes in the log domain for three pixels “in tungsten" (i.e., pixels like the bar patterns observed in Figure 2.5 for which the measurements are lower than expected because the rays reaching it

primarily pass through a tungsten slit) and the neighboring "air" regions, in order of increasing tungsten slit size. Though beam hardening generally leads to a non-linear effect, the measurements are mostly linear but with different slopes for different positions, suggesting that the effective beam energy is changing. While the slope estimated for all three air points is similar, the slopes estimated "in tungsten" tended to decrease with increasing tungsten slit size. The increased tungsten slit size causes increased penetration through tungsten and more beam hardening, thus resulting in a greater effective beam energy, which is consistent with a smaller slope in the log-domain.

The difference in slopes for pixels corresponding to rays "in air" and "in tungsten" give rise to a spectral coefficient β which can then be used to correct the line integral data $-log(y/M)$. The measurement model for the PMMA calibration scans follows

$$\bar{P}(u) = G(u)\left(B' * M(u)\right) e^{-\beta(u) t_p(u)} \tag{2.8}$$

where β is the spatially-varying first-order spectral correction factor to be estimated, t_p is the PMMA thickness and B' is a distinct blur from B in 2.1 that needs to be corrected by a separate blur correction in order to match the MAD state in the PMMA scans to the projection data Y.

The full measurement model for Y now becomes

$$\bar{Y}(u) = G(u)\left(B * M(u)\right) e^{-\hat{\beta}(u) l(u)} \tag{2.9}$$

where

$$\hat{\beta}(u) = \hat{k}(\beta(u) - \bar{\beta}) + 1 \tag{2.10}$$

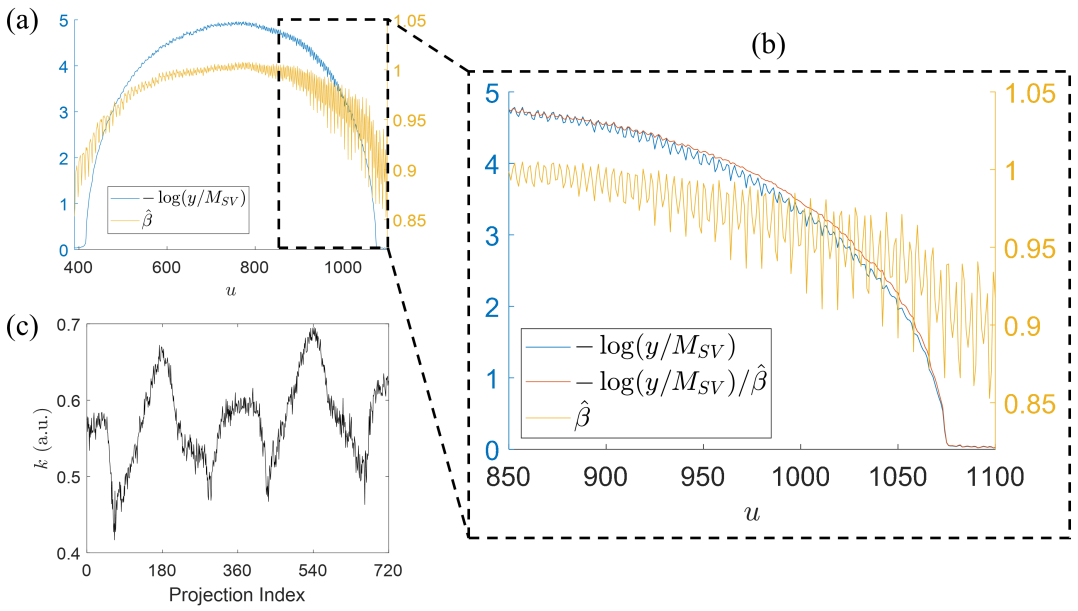

Figure 2.7: (a - b) Line profiles of log-domain projection data, estimated spectral correction factor $\hat{\beta}$ and spectral corrected data. (c) Estimated k per projection for elliptical phantom.

is the spectral coefficient that differs from the measured β by a global scaling parameter, $\hat{k}$, because the measured slope in the PMMA calibration scans contain the inherent attenuation coefficient of PMMA. The estimated slopes for every point on the detector must therefore be divided by the spatial mean $\bar{\beta}$ to find the spectral coefficient β. $\hat{k}$ is chosen according to

$$\hat{k} = \arg\min_{k} \text{Std}\left\{\nabla\left\{\frac{-\log(y(u)/M_{SV}(u))}{k(\beta(u)-\bar{\beta})+1}\right\}\right\} \tag{2.11}$$

where ∇ is the discrete gradient operator and Std $\{\nabla\{\cdot\}\}$ seeks to minimize the high frequency MAD content in the line integral domain. Here, k is a data-dependent scaling of β that keeps the spatial mean equal to one but chooses a mean effective energy for the data which is artifact free. In practice, this optimization is again performed per frame by averaging rows in the object region to reduce noise.

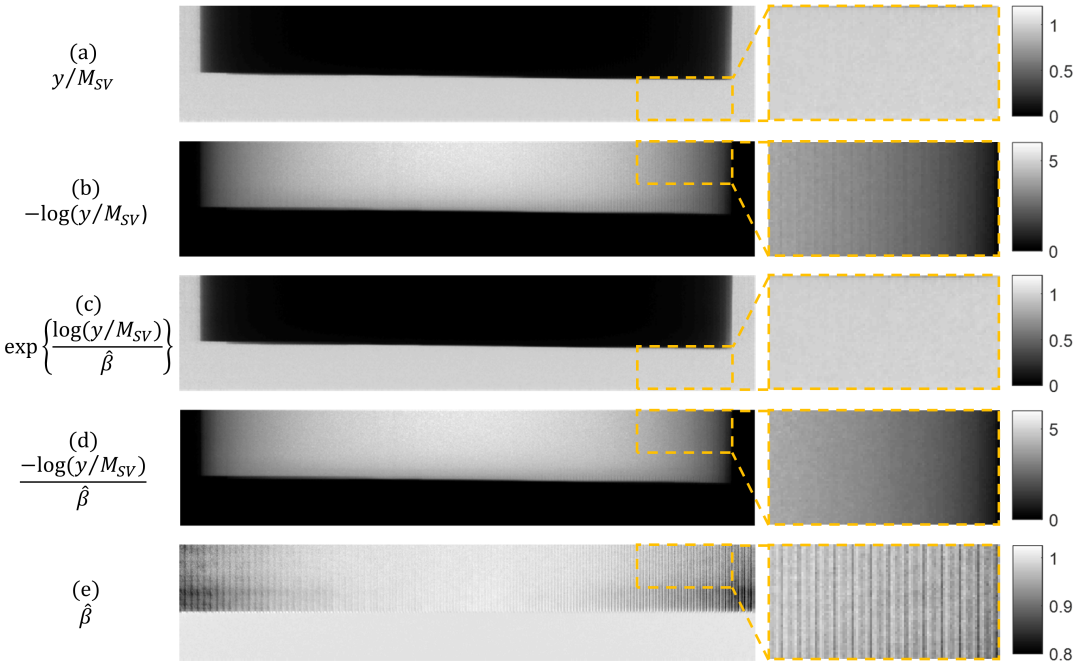

Figure 2.8: Comparison of spectral correction results for the long-axis projection of an elliptical phantom on pre-log and log scales. (a-b) Shift-variant blur corrected projection, (c-d) shift-variant blur correction with spectral correction factor $\hat{\beta}$ shown in (e).

Once βs have been measured and $\hat{k}$ computed, the line integrals in the object region are corrected by

$$l(u) = \frac{-\log\{y(u)/M_{SV}(u)\}}{\hat{\beta}(u)} \tag{2.12}$$

The results of the spectral correction process for the elliptical phantom are summarized in Figures 2.7 and 2.8. As seen in Figures 2.7b and 2.8d, the combination of blur and $\hat{\beta}$ spectral correction visibly reduces the high-frequency bar patterns present in the line integral data. As indicated by Figure 2.7c, the optimal scaling factor $\bar{k}$ is data-dependent.

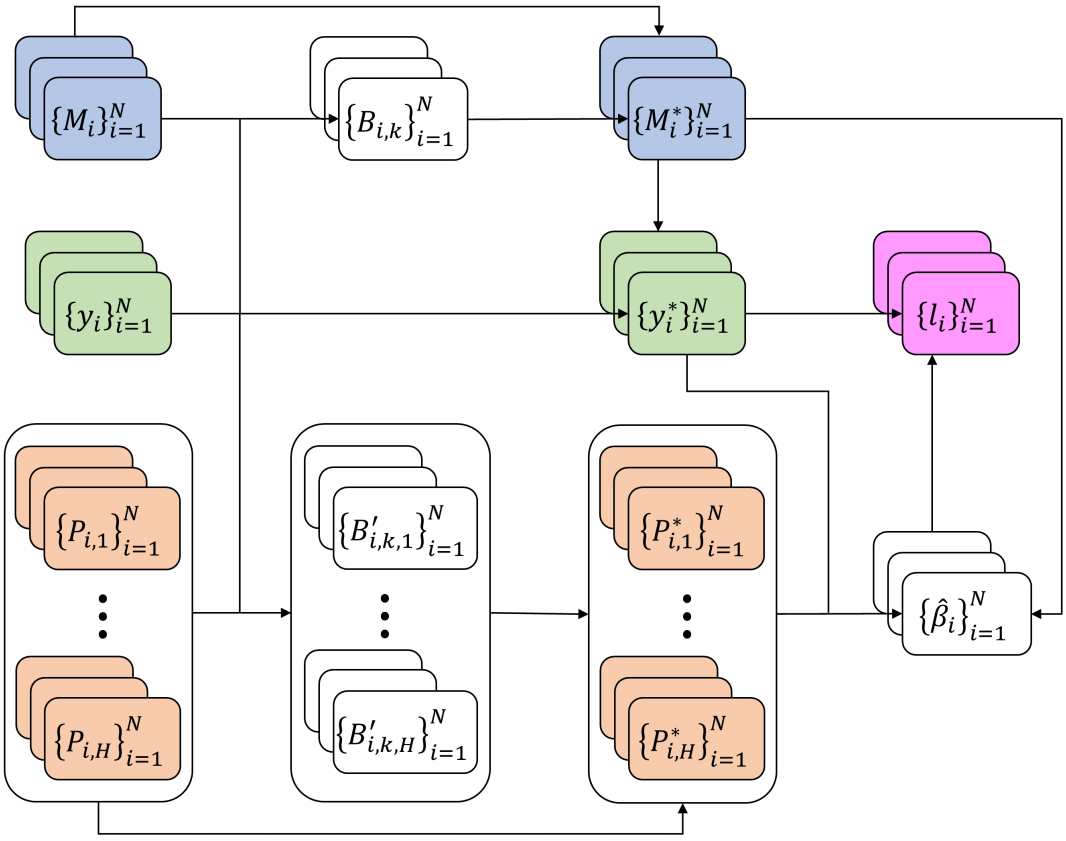

Figure 2.9: MAD correction flowchart. The projection data y along with the two sets of calibration scans M and P are each highlighted in distinct colors. N is the number of frames in the acquired data which may each correspond to a different MAD position, so N is therefore matched between all three sets of scans. Each frame is corrected separately.

2.4 Full Correction Model

The overall MAD reconstruction workflow as presented is summarized in Figure 2.9. The gain corrected data y is used jointly with M to estimate a set of blur kernels B to obtain the blur corrected MAD transmissivity M^*, which yields the MAD corrected data y^*. $P_1 \dots P_H$, which denote the PMMA calibration scans of varying thickness, also undergo a blur correction process to yield $P_1^* \dots P_H^*$. Dividing $P_1^* \dots P_H^*$ by M^* and combining with y^*, which are all matched in focal spot state, allows estimation of $\hat{\beta}$. Combining y^* with

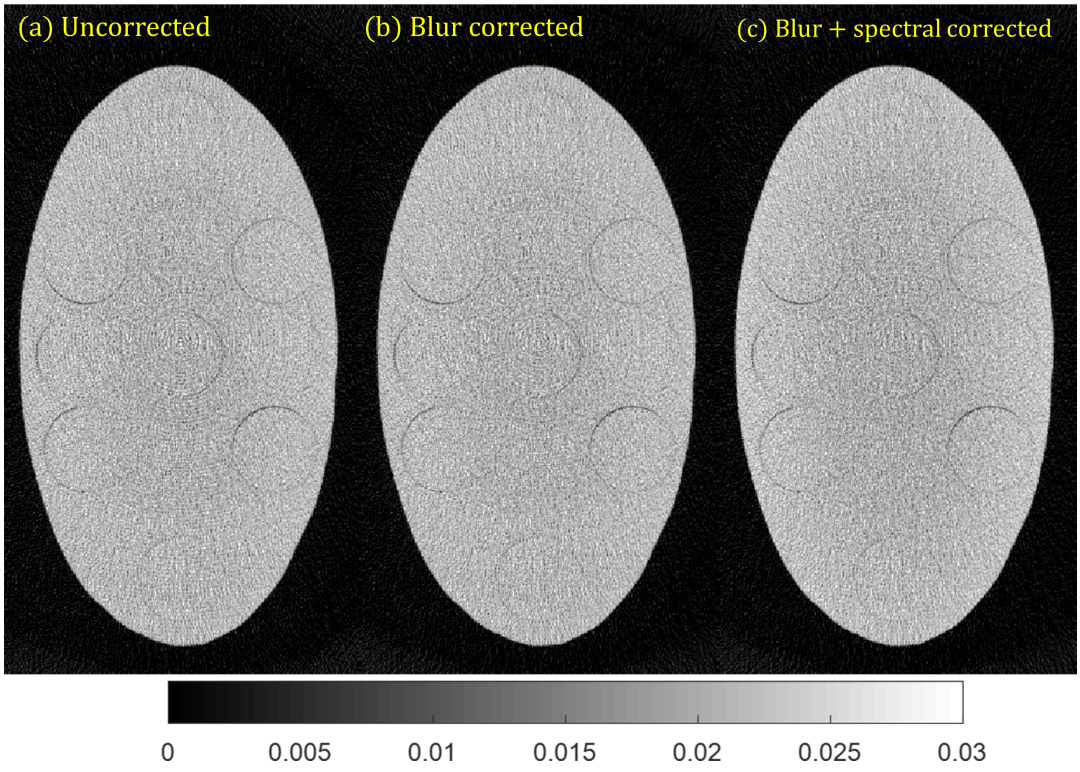

Figure 2.10: Comparison of uncorrected (a), blur corrected (b) and fully corrected (c) FDK reconstructions.

$\hat{\beta}$ yields the final corrected line integrals l, which can be used as input to the reconstruction algorithm.

A comparison of the FDK reconstructed images for the uncorrected, blur corrected (only) and fully corrected methods is shown in Figure 2.10. As expected, blur correction lessens the appearance of but does not completely eliminate the ring artifacts, while the full correction model offers the greatest reduction in ring artifact magnitude.

2.5 Discussion

While the correction process described in this chapter was largely successful in reducing the ring artifacts associated with MAD-based FFM, there are several unanswered questions that remain. In particular, the blur kernel optimization process used in this work is completely unconstrained with w free parameters per segment. To make this estimation process more consistent with the physical model of the blooming or shifting focal spot, a parametric blur model which uses assumptions of smooth variations spatially and temporally should be pursued. This should also make the estimation process more robust to noise in the data.

Additionally, the use of a first-order spectral correction factor may yield sub-optimal results, as inspection of Figure 2.7a suggests there may be a nonlinear effect. While the spectral calibration was performed on an object of similar material to the object scanned, the spectral properties may differ more significantly for an object with very different composition (e.g., bone), which may affect the correction performance. Finally, the effect of the MAD correction process on image quality (e.g., noise properties or spatial frequency content) has not been properly studied here, though initial work on this matter has been presented in Gang et al. (2018 (accepted)[a]), Gang et al. (2018 (accepted)[b]), and Gang et al. (2018 (submitted)).

References

Stayman, J. Webster, Aswin Mathews, Wojciech Zbijewski, Grace Gang, Jeffrey Siewerdsen, Satomi Kawamoto, Ira Blevis, and Reuven Levinson (2016). "Fluence-Field Modulated X-ray CT using Multiple Aperture Devices". In: *Proc. of SPIE Medical Imaging 2016: Physics of Medical Imaging* 9783, pp. 97830X1–6. DOI: 10.1117/12.2214358.

Mathews, A. J., S. Tilley, G. Gang, S. Kawamato, W. Zbijewski, J. H. Siewerdsen, R. Levinson, and J. W. Stayman (2016). "Design of dual multiple aperture devices for dynamical fluence field modulated CT". In: *Conf Proc Int Conf Image Form Xray Comput Tomogr* 4, pp. 29–32.

Hsieh, Jiang. *Computed Tomography Principles, Design, Artifacts, and Recent Advances*. Vol. 1. SPIE.

Gang, Grace J., Andrew Mao, Wenying Wang, Jeffrey H. Siewerdsen, Aswin Mathews, Reuvin Levinson, and J. Webster Stayman (2018 (accepted)[a]). "Dynamic Fluence Field Modulation with Multiple Aperture Devices: Design, Implementation, and Assessment". In: *The 60th Annual Meeting of the AAPM, Nashville, TN, USA*.

Gang, Grace J., Andrew Mao, Jeffrey H. Siewerdsen, and J. Webster Stayman (2018 (accepted)[b]). "Implementation and Assessment of Dynamic Fluence Field Modulation with Multiple Aperture Devices". In: *The Fifth International Conference on Image Formation in X-ray Computed Tomography, Salt Lake City, UT, USA*.

Gang, Grace J., Andrew Mao, Wenying Wang, Jeffrey H. Siewerdsen, Satomi Kawamoto, Reuvin Levinson, and J. Webster Stayman (2018 (submitted)). "Dynamic fluence field modulation in CT with multiple aperture devices". In: *The 104th Annual Meeting of the RSNA, Chicago, IL, USA*.

Chapter 3

Patient Miscentering

As discussed in Chapter 1, traditional CT image acquisition uses bowtie filters to reduce dose, x-ray scatter, and detector dynamic range requirements. To make use of traditional bowtie filters, patients must be centered within the scanner. However, accurate patient centering within the bore of the CT scanner takes time and is often difficult to achieve precisely. Patient miscentering, combined with a static bowtie filter can result in significant increases in dose, reconstruction noise, and CT number variations and consequently raising overall exposure requirements. This chapter presents a new approach to estimate the patient's position from scout scans and a method to perform dynamic spatial beam filtration during acquisition. In physical experiments, we demonstrate improved dose utilization and more consistent image performance with dynamic beam filtration as compared to the unmodulated baseline, which has the potential to relax patient centering requirements, reduce set-up time, and facilitate additional CT dose reductions. The material found in this chapter is largely reproduced from the work in Mao et al. (2018) and Mao et al. (2018 (submitted)).

3.1 Introduction

A common technique for dose reduction in x-ray CT is the use of bowtie filters. These filters typically shape the x-ray beam spatially through selective attenuation to decrease the fluence incident to the patient for measurements expected to have lower attenuation. Consequently, this reduces the exposure for measurements that do not require high fluence. More specifically, bowtie filters are often designed to flatten the fluence profile arriving at the detector (Toth et al., 2005; Wunderlich and Noo, 2007). However, clinical CT scanners use static filtration without the ability to translate the bowtie filter. This results in poor dose utilization, reduced image quality, and CT number variations (e.g., due to artifacts) when the patient is not well-centered within the bore (Toth, Ge, and Daly, 2007; Habibzadeh et al., 2010; Szczykutowicz, DuPlissis, and Pickhardt, 2017). Toth et. al. have reported that patients are routinely miscentered in elevation by an average of 2.3 cm and up to 6 cm clinically. In those studies, miscentering of 3 cm and 6 cm showed an 18% and 41% increase in dose and a 6% and 22% increase in noise, respectively (Toth, Ge, and Daly, 2007).

Similar concerns arise in emergency medicine where physicians often have 1) limited prior knowledge of the location of potential disease and therefore need to visualize the entire body volume with high image quality; and 2) limited time to properly position the patient. For these reasons, emergency room (ER) CT scanners often operate without a bowtie, thus forgoing the dose-saving benefits of beam filtration. While techniques have been developed for automatic centering that involve readjusting the patient in the bore (Li

et al., 2007), both miscentering in ordinary diagnostic CT and bowtie-free ER scanning would benefit greatly from a method to dynamically position the beam filter during acquisition, thereby improving the overall efficiency of the CT examination without disrupting the clinical workflow.

This work presents a general method to calculate actuation profiles for various types of dynamic beam filters based on two low-dose "scout" scans of the patient (i.e., topograms). Such scout images are routinely obtained for positioning to ensure the region-of-interest is in the field-of-view (FOV) (Li et al., 2014), to reasonably center patients (Mayo-Smith et al., 2014), and to determine an appropriate x-ray technique and other acquisition parameters (Lambert et al., 2015; Hara et al., 2013).

In the following sections we describe strategies to drive dynamic beam modulation for miscentered patients based on knowledge of the set of beam patterns achievable with a given modulation strategy as well as scout scan data. We demonstrate the methodology in physical experiments using three beam filtration approaches: 1) a traditional aluminum bowtie filter with the capability of lateral translation; 2) a single-MAD beam filter (MAD0 only) with lateral translation; and 3) a dual-MAD filter with two independently actuated filters that permits additional control over the center and width of the beam profile. Image quality and dose are compared for both static and dynamic modulation strategies.

3.2 Methods

3.2.1 Patient Position Estimation

To optimize beam modulation, some form of patient model is required to predict the attenuation along different measurement ray-paths. To estimate the patient position within the FOV, we propose a parametric model for the patient/object shape, $o(\Omega)$, in the central axial plane as a rectellipse function as illustrated in Figure 3.1. The rectellipse is similar to the ellipse in that it has parameters describing its center position (x_c, y_c), width w, and height h (in units of voxels). However, the rectellipse also includes a shape parameter c for a continuously variable shape between $c = 0$, an ellipse, and $c = 1$, a rectangle. Additional parameters define a uniform attenuation coefficient μ and a rotation angle about the center R. Mathematically, the parameterized object is given by the quartic Cartesian equation

$$\left(\frac{i}{w}\right)^2 + \left(\frac{j}{h}\right)^2 - c^2\left(\frac{ij}{wh}\right)^2 \leq 1 \tag{3.1}$$

where

$$\begin{bmatrix} i \\ j \end{bmatrix} = \begin{bmatrix} \cos(R) & -\sin(R) \\ \sin(R) & \cos(R) \end{bmatrix} \begin{bmatrix} x - x_c \\ y - y_c \end{bmatrix} \tag{3.2}$$

represent the translated and rotated coordinates of x and y in the axial plane respectively (Guasti, 1992).

Low-dose scouts of the patient are acquired at the two orthogonal anteroposterior (AP) and lateral (LAT) views. Measurements from the central detector row are used to form a data vector g. The seven parameter object model $\Omega = \{x_c, y_c, w, h, c, \mu, R\}$ is then optimized by minimizing the mean

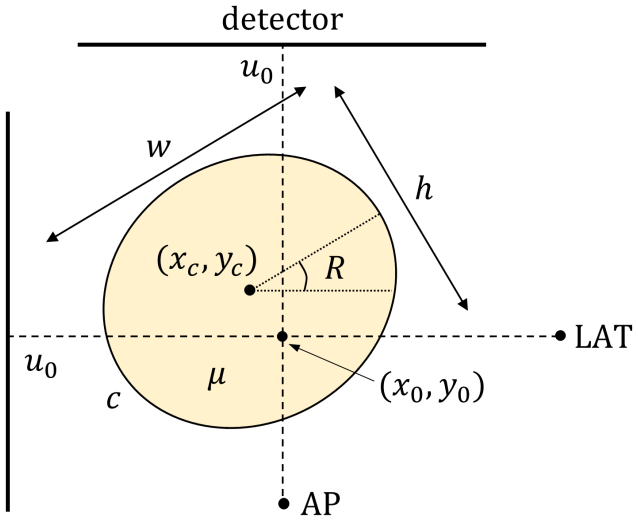

Figure 3.1: (Geometry for object calibration showing the parametric rectellipse model in the central axial plane and the positions at which the two scout scans of the object are acquired.

squared difference between the forward projected object and g, according to

$$\hat{\Omega} = \arg\min_{\Omega} \|\mathbf{P}o(\Omega) - g\|_2^2 \tag{3.3}$$

where $\mathbf{P}$ is the fan-beam forward projector of x that generates the AP and LAT views using the Siddon approach (Siddon, 1984). The optimization in (3.3) is non-convex and does not readily admit a closed-form solution. In this work, this problem is solved using the Nelder-Mead search method (Nelder and Mead, 1965) using initializations of the height, width and center parameters obtained by simple thresholding of the orthogonal projections and computing the centroid, where the object is initially assumed to be elliptical ($c = 0$), be minimally rotated with respect to the scanner axes, and has an attenuation coefficient close to that of soft tissue at the mean x-ray beam energy $\bar{E}$. The parameters $\Omega_1 = \{x_c, y_c, w, h\}$ are optimized first to obtain a good positional estimate, before optimizing $\Omega_2 = \{\mu, c, R\}$ while holding Ω_1

constant to match the magnitude, curvature and asymmetry of the projections respectively. Then, the entire parameter set Ω is optimized together to obtain the final object parametrization. While more robust algorithms for global non-convex optimization may be applied, this heuristic optimization approach was found to be efficient and practical for the rectellipse problem.

From the calibrated object, the amount of patient miscentering in the AP and LAT views can be computed according to the equations

$$\begin{aligned} e_{\text{ap}} &= (x_c - x_0)a_x \\ e_{\text{lat}} &= (y_0 - y_c)a_y \end{aligned} \tag{3.4}$$

respectively, where a_x, a_y are the natural voxel sizes in the axial plane and x_0, y_0 are both the center coordinates of the object image and the center of object rotation.

3.2.2 Filter Calibration

In order to design the filter actuations for dynamic beam filtration, the available beam profiles must be characterized. Consider the case of a traditional bowtie filter based on variable attenuation of a uniform material. Given the source-to-filter distance (SFD) in the scanner (which is assumed to be fixed and parallel to the imaging plane) and the design specifications of the beam filter (i.e., the thickness of the bowtie $h(x)$ at discrete points x along its width), the expected modulation pattern at the detector $f(u;t)$ (where u is the positional index across the detector) for a specified translation t can be calculated analytically based on ray tracing. This geometry is illustrated in Figure 3.2.

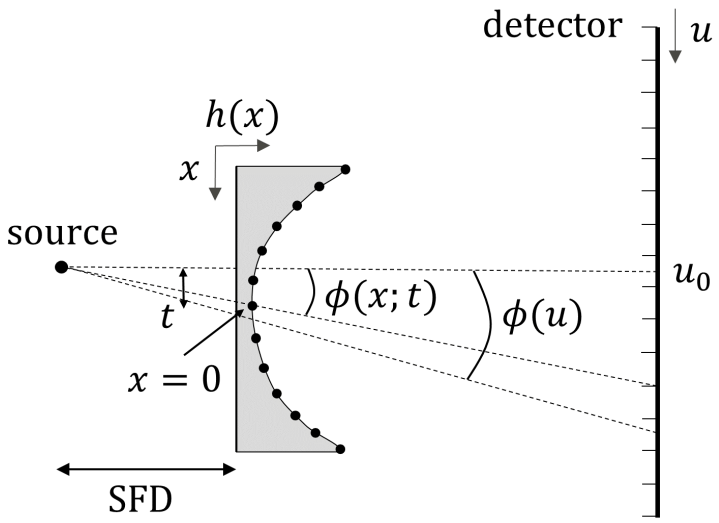

Figure 3.2: Geometry for calculating the bowtie transmissivity. Tracing the ray through known points along the length of the bowtie, shown as black dots, yields line integral measurements at an angular sampling different than that of the detector. The translation t shifts the origin of the x coordinate, where $x = 0$ is at the center of the bowtie and assumed to be aligned with isocenter (u_0 is the central detector element) with no filter translation.

The path length l of a ray traveling through the bowtie at lateral position index x to reach the angular sampling position ϕ at the detector for a translation t, assuming no re-entrant crossings, is given by

$$l(\phi(x;t)) = \frac{h(x;t)}{\cos(\phi(x;t))} \tag{3.5}$$

$$\phi(x;t) = \tan^{-1}\left(\frac{x+t}{SFD + h(x;t)}\right) \tag{3.6}$$

Line integrals through the filter may be estimated using a monoenergetic forward model with knowledge of the bowtie material and attenuation coefficient, μ, and the mean x-ray beam energy, $\bar{E}$. For this work, these physical quantities were estimated using *Spektr* (Punnoose et al., 2016), a computational tool for x-ray spectral analysis, and the known physical settings for the x-ray test bench. Piecewise cubic Hermite interpolating polynomials were used to

find estimates on the detector for particular angular samples $\phi(u)$, followed by exponentiation to yield the expected bowtie transmissivity,

$$f_b(t) = \exp\left\{-\mu(\bar{E})l(\phi(u;t))\right\} \tag{3.7}$$

where we have dropped the explicit dependence of f on u for notational convenience.

However, $f(t)$ is not straightforward to compute in MAD-based filtering due to obliquity effects. That is, even though the filters are relatively then, the MAD slits act as a focused grid and translation of the MADs away from the center will narrow the beam. $f(t)$ may alternatively be estimated through a calibration scan which can be conducted by discretely translating the filter through the range of achievable motion and then interpolating to find the modulation patterns at specific actuation positions. We have performed such a calibration scan for both single- and dual-MAD filtration setups on our CT test bench. The MAD calibration results are summarized in Figure 3.3 and include an illustration of the fluence function computed for a translating aluminum bowtie filter. The single-MAD calibration was conducted using 0.125 mm steps over approximately 7 cm. For the dual-MAD setup, MAD0 was actuated in 0.1 mm increments with relative displacements of MAD1 using 0.05 mm increments over one period (approximately $\pm$0.45 mm) at each MAD0 position. MAD calibration scans were smoothed with an additional low-pass filtering step (using a Butterworth IIR low-pass filter) to avoid fitting residual high-frequency spatial modulations created by the MAD. Interpolation using splines was applied to obtain $f(t)$ at arbitrary actuation positions. Note that

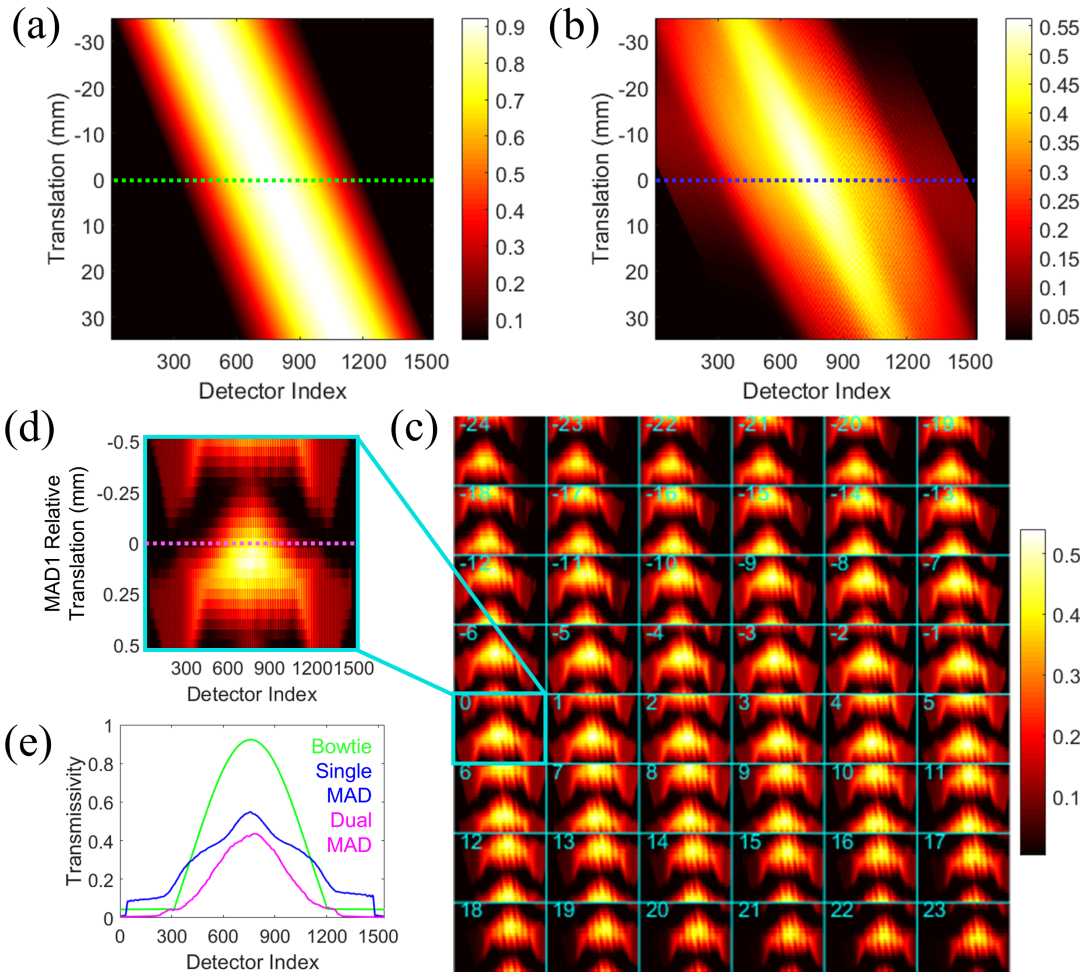

Figure 3.3: Fluence functions for the three beam modulation strategies: (a) Computed fluence for a translating aluminum bowtie $f_b(t)$; (b) measured fluence patterns for a single-MAD $f_s(t)$; and (c) measured fluence patterns for dual-MAD filters $f_d(t)$. For the dual-MAD setup, the absolute translation of MAD0, in millimeters, is labeled in the top left of each cell in (c). The profiles achievable within approximately one period of relative MAD1 translation for the centered MAD0 position are shown in (d). (e) Comparison between the central line profiles $f(0)$ of the three filters (labeled by the dotted lines), where the fluence levels are, in general, lower but broader for the single-MAD filter than the bowtie, and lowest for the dual-MAD filter. All images and plots are normalized based on fluence without filters.

the range and spacing of actuations that need to be sampled during this calibration is dependent on where the object and MADs are placed in the field of view. The SFD for the test bench scanner is $\sim$ 39 cm, whereas in a commercial scanner, the MADs would be placed much closer to the source

(e.g., $\sim$ 15 cm), requiring finer sampling but less total actuation.

In general, translation of the filter controls the centering of the beam for the bowtie and single-MAD filters. For the dual MADs, the centering is controlled by the absolute translation of MAD0, but additional capability for beam width control is conferred by the relative translation of MAD1 with respect to MAD0. For both the single- and dual-MAD filters, however, there is additional variation in beam width and amplitude as a function of absolute displacement owing to obliquity effects. That is, even though the filters are relatively thin, the MAD slits act like a focused grid and translation of the MADs away from the center will narrow the beam. Such beam narrowing is evident in Figure 3.3b and 3.3c.

3.2.3 Filter Trajectory Calculation

Combining the patient/object model with the achievable fluence functions from the previous section permits estimation of the actuation required to drive the dynamic filters. Mathematically, multiplying f with the forward projection of $o(\hat{\Omega})$ (from Section 3.2.1) yields the expected detector fluence p as a function of t:

$$p(t;\theta) = f(t)e^{-\mathbf{P}(\theta)o(\hat{\Omega})} \tag{3.8}$$

where $\mathbf{P}(\theta)$ is the Siddon fan-beam forward projector applied to $o(\hat{\Omega})$ at projection angle θ. We choose to estimate the optimal translation of the filter $\hat{t}$ at each individual projection θ_i, where $i \in \{0, 1, \ldots, N-1\}$, which is a low-dimensional optimization of $p(t;\theta_i)$ over t. To compute $\hat{t}(\theta_i)$, we consider several possible design approaches:

1. *Center Matching (CM)*: Analytically match the ray passing through the center of the object with the center of the beam filter at the SFD, given by

$$\hat{t}(\theta_i) = SFD\frac{r\cos(\theta_i - \phi)}{SAD + r\sin(\theta_i - \phi)} \tag{3.9}$$

where r and ϕ describe the distance and orientation of the object center with respect to the image origin, respectively, as shown in Figure 3.4. Mathematically,

$$\begin{aligned} r &= \sqrt{a_x^2(x_c - x_0)^2 + a_y^2(y_c - y_0)^2} \\ \sin\phi &= a_x\frac{x_c - x_0}{r} \\ \cos\phi &= a_y\frac{y_0 - y_c}{r} \end{aligned} \tag{3.10}$$

which may be substituted into (3.9) by application of the trigonometric

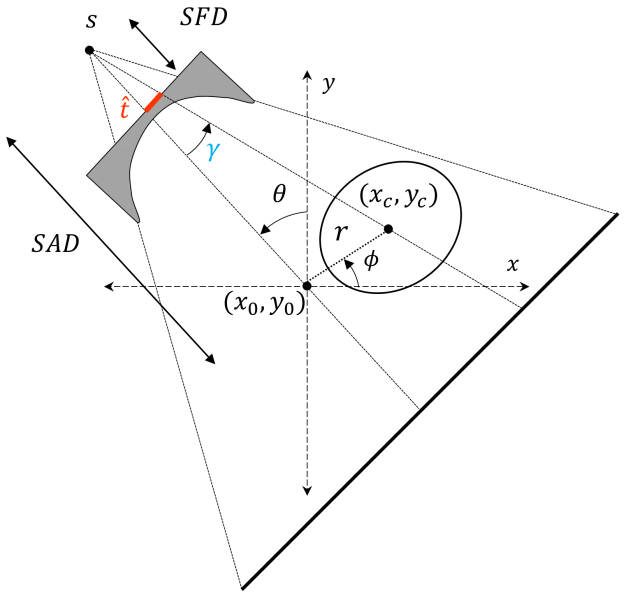

Figure 3.4: Geometry of the CM trajectory design method. Finding the tangent of the fan-beam ray γ (blue) allows simple computation of the filter actuation $\hat{t}$ (red).

angle addition formulas. The right hand term in (3.9) represents the tan term for the fan-beam ray γ passing through the center of the object at gantry rotation angle θ_i. The full derivation for this expression can be found in Kak and Slaney 2001 (Kak and Slaney, 2001).

2. *Minimum Standard Deviation (MSD)*: Minimize the spatial standard deviation of the expected detector fluence via the following optimization:

$$\hat{t}(\theta_i) = \underset{t \in \mathcal{T}(\theta_i)}{\arg\min} \, \mathrm{Std}_{\mathrm{Y}} \left\{ p(t; \theta_i) \right\} \tag{3.11}$$

where $\mathrm{Std}\{\cdot\}$ computes the spatial standard deviation of the detector signal. Y is a support region for the calculation where either a) $\mathrm{Y} = U$, the "full-field" case where U is the entire horizontal detector extent, or b) $\mathrm{Y} = \Phi(\theta_i)$, where $\Phi(\theta)$ denotes measurements at angle θ containing only the object (e.g., $\Phi(\theta) = \{u \mid e^{-\mathbf{P}(\theta) o(\hat{\Omega})} < 1\}$). This generates two distinct strategies which we refer to as MSD-U and MSD-O respectively.

3. *Normalized Minimum Standard Deviation (NMSD)*: Minimize the ratio of the spatial standard deviation of the expected detector fluence to its spatial mean, according to

$$\hat{t}(\theta_i) = \underset{t \in \mathcal{T}(\theta_i)}{\arg\min} \, \frac{\mathrm{Std}_{\mathrm{Y}} \left\{ p(t; \theta_i) \right\}}{\mathrm{Mean}_{\mathrm{Y}} \left\{ p(t; \theta_i) \right\}} \tag{3.12}$$

where $\mathrm{Mean}\{\cdot\}$ is the spatial mean operator. We again denote the two separate strategies referring to the choice of Y as NMSD-U and NMSD-O respectively.

For the optimizations in (3.11) and (3.12), $\mathcal{T}$ is a convex set which varies depending on the filtration strategy. For the 1DOF filters (i.e., the bowtie and single-MAD filters),

$$\mathcal{T}_1(\theta_i) = \begin{cases} \{t \in \mathbb{R} \mid |t - t(\theta_{i-1})| \leq \epsilon\} & \theta_i \neq \theta_0 \\ \mathbb{R} & \theta_i = \theta_0 \end{cases} \tag{3.13}$$

where the parameter ϵ is a hard constraint on the magnitude of the shift in absolute filter position at each angular step after the starting angular position θ_0 to promote overall trajectory smoothness. For the 2DOF filter (i.e., the dual MAD),

$$\mathcal{T}_2(\theta_i) = \begin{cases} \left\{t \in \mathbb{R}^2 \mid |t - t(\theta_{i-1})| \leq \begin{bmatrix} \epsilon & \eta \end{bmatrix}^T \wedge \min_{u \in \Phi(\theta_i)} f(t) > \lambda\right\} & \theta_i \neq \theta_0 \\ \left\{t \in \mathbb{R}^2 \mid \min_{u \in \Phi(\theta_i)} f(t) > \lambda\right\} & \theta_i = \theta_0 \end{cases} \tag{3.14}$$

where $t = \begin{bmatrix} t^0 & t^1 \end{bmatrix}^T$ are the absolute MAD0 and MAD1 translations respectively and $|\cdot|$ is the element-wise absolute value function. The quantity λ is a hard minimum transmissivity constraint within Φ to avoid imaging through the low MAD transmissivity region ($\sim$ 2% as seen in Figure 3.3e), where the scatter-to-primary ratio is likely to be very high and would contribute to significant image artifacts—as demonstrated in previous studies of the effect of bowtie filters on CT image quality (Mail et al., 2008; Xu et al., 2016). In this study, $\epsilon = 1$ mm, $\eta = 0.1$ mm and $\lambda = 0.05$ (5%). Due to these definitions of $\mathcal{T}_1$ and $\mathcal{T}_2$, the trajectory optimizations can be solved quickly even by brute-force search.

The CM approach (3.9) simply attempts to match the center of the filter and the center of the object, which reduces to the solution of a similar triangles

problem. The MSD method (3.11) is a uniform fluence objective which seeks to find the modulation profile that will have the lowest spatial variation in signal at the detector. Such an objective will also tend to homogenize noise, since variance is dominated by primary quantum noise which is Poisson and proportional to signal level. The NMSD objective (3.12) modifies (3.11) to prefer higher mean fluence arriving at the detector. This is because while low spatial variation may be desired, using low overall fluence to achieve flatness is not desirable. By considering the ratio of spatial standard deviation to the mean signal levels, we may avoid trivial solutions where the fluence is simply zero. Such patterns are achievable with dual MADs due to the second degree of translation freedom.

The five candidate metrics (CM, MSD-U, MSD-O, NMSD-U, and NMSD-O) were individually analyzed and used to identify a single best design objective for each of the three beam filtration strategies used in this study. The selected trajectory design strategies were then used to carry out the physical experiments outlined in the following section.

3.2.4 Experiments

3.2.4.1 CT Benchtop with Filter Motion Stages

Dynamic beam filtration was implemented on a CT test bench, shown in Figure 3.5. The test bench includes a Varex 4343CB amorphous silicon flat-panel detector, a Varex Rad-94 x-ray tube (Palo Alto, CA, USA) with an added 2 mm Al and 0.2 mm Cu of beam filtration, a 6-axis Hexapod for object rotation (ALIO Industries, Arvada, CO, USA) and two Velmex XSlide linear motion

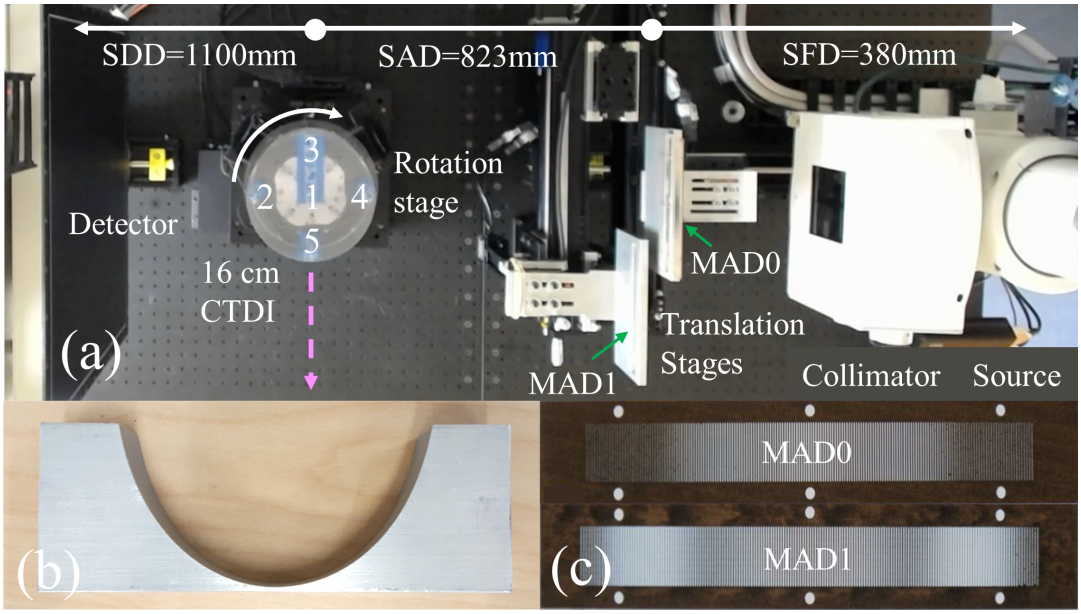

Figure 3.5: (a) CT test bench with dual MADs indicated by the green arrows. CTDI dosimeter locations are numbered and the pink dotted arrow indicates the direction of left miscentering. (b) Aluminum bowtie and (c) MAD filter.

stages for filter positioning (Bloomfield, NY, USA). Actuation of the rotation and linear motion stages was synchronized with the x-ray source pulsing to perform step-and-shoot image acquisitions (i.e., the filters move into position before each frame of acquisition). The system geometry was chosen to emulate the source-to-detector distance of a clinical CT scanner and to be consistent with the geometry for which the MADs were designed for (Stayman et al., 2016; Mathews et al., 2016), with an SFD of 380 mm, a source-to-axis distance of 823 mm to maximize the FOV, and source-to-detector distance of 1100 mm.

3.2.4.2 Image Quality Studies

To investigate the performance of the above methods in mitigating the dose and image noise penalties of miscentering, experiments were conducted with

a 16 cm CTDI phantom—a uniform PMMA cylinder which mimics the size and attenuation of the human head. The CTDI phantom was scanned with miscentering of approximately 0, 2, and 4 cm toward the left side of the detector for both static (no filter actuation) and dynamic filter positioning for three beam filtration strategies: an aluminum bowtie, a single-MAD (shown as MAD0 in Figure 3.5a), and the dual-MAD filters. For each combination of miscentering and beam filter, the static beam position was set to be the mean absolute translation of the dynamic trajectory. Mathematically, the actuation position was computed as

$$t_{\text{static}} = \frac{1}{N} \sum_{\theta} \hat{t}(\theta) \tag{3.15}$$

where N is the number of angular projections. For the dual-MAD case, the relative MAD1 translation that minimized the design objective for the mean MAD0 position was used.

Scout scans were acquired from single cone-beam projections at the AP and LAT views using 100 kV and 0.256 mAs. Image acquisition was performed with $N = 360$ projections over a full 360° rotation (with a constant angular step) at 100 kV, 92 mAs (0.256 mAs/projection), and 10°/15° vertical beam collimation (cone angle) for dose/noise measurements, respectively. The design of the aluminum bowtie was optimized for the CTDI phantom at 100 kV, whereas the MADs were designed to flatten the fluence for a wide range of object diameters (Stayman et al., 2016; Mathews et al., 2016). Because fluence levels differ between filters and with translation and are not simply scaled versions of each other (as is apparent from Figure 3.3), the acquisitions

using different beam filters were not dose matched.

Dose measurements were made in the 16 cm CTDI phantom using a Radcal 6 cc gas ionization chamber (Model 10x6-0.6, Monrovia, CA, USA). The accumulated dose over a full 360° projection scan for each dosimeter location (as labeled in the CTDI phantom in Figure 3.5a) d_j was measured, and the weighted dose was calculated using the standard weighted average of central and peripheral dose:

$$CTDI_w = \frac{1}{3}d_1 + \frac{2}{3}\frac{\sum_{j=2}^{5} d_j}{4} \tag{3.16}$$

The % difference in the dose measurement with respect to the centered condition was then computed to investigate the change as a function of the amount of miscentering.

To analyze noise, two sequential data acquisitions were performed and reconstructed with the Feldkamp (FDK) algorithm (Feldkamp, Davis, and Kress, 1984). Difference images were formed to create noise-only image volumes with a $1/\sqrt{2}$ correction factor applied. Regions-of-interest (ROIs) of 31x31x7 voxels were defined for each of the 5 dosimeter locations in the central volume of the difference image and used to quantitatively assess the standard deviation of voxel values σ_j. Additionally, a 7x7x7 voxel box standard deviation filter was convolved with the difference image. The central axial slice of the result was used to qualitatively assess the noise distribution within the object. The spatial mean of the noise over this noise map was computed and defined as σ_w. The % difference (from the centered object scenario) was again used to assess the effect of beam modulation on the noise measurements.

From the noise maps, the "noise-adjusted" exposure level (Toth, Ge, and Daly, 2007) – the % dose change needed to maintain the same peak variance as the centered case – was calculated assuming the dose should be increased by an amount proportional to the square of the peak noise increase. That is, presuming that the noise is dominated by photon statistics (i.e., low electronic noise) permits a scaling of the exposure (and therefore dose). For a global image quality measure, peak variance was used, as in related studies (Hsieh and Pelc, 2014; Hsieh, Fleischmann, and Pelc, 2014). This presumes all portions of the image volume are subject to the same maximum noise constraint and is consistent with diagnostic tasks for which the location of disease/defects is unknown.

3.2.4.3 Anthropomorphic Head Phantom Study

CT scans were also conducted of an anthropomorphic head phantom (CIRS ATOM Head Partial Phantom Slice #6, Model 701-HN, Norfolk, VA, USA) under centered and miscentered conditions to investigate an anatomical imaging case with a miscentered, non-uniform and non-circular object. The dual-MAD filter was chosen for this experiment as its width modulation capability is appropriate for elliptically shaped, anthropomorphic objects. Scouts were obtained at 100 kV and 0.512 mAs, and images were acquired at 100 kV and 184 mAs (0.512 mAs/projection) with 15° vertical beam collimation. Noise was qualitatively analyzed in a similar manner to that described before but computed only over voxels interior to the patient. A patient mask was identified using a segmentation based on Otsu's binary threshold algorithm (Otsu, 1979). Additionally, the computed axial noise maps were each normalized

by the mean value over the entire interior head region for comparison on a common window level.

For this study, we focused on the NMSD-O design strategy. The static beam profile was the same across both the centered and miscentered cases. The MAD0 position t^0_{static} was again defined according to (3.15) using the miscentered trajectory, and the relative MAD1 translation was selected by finding the fluence pattern that minimizes the sum of the objective in (3.12) for the miscentered object $o(\hat{\Omega}_M)$ over all angular projections, i.e.

$$t^1_{\text{static}} = \underset{t^1 \in \mathcal{T}_{\text{static}}}{\arg\min} \sum_{\theta} \frac{\text{Std}_{\Phi(\theta)} \left\{ p(t^1; t^0_{\text{static}}, \hat{\Omega}_M, \theta) \right\}}{\text{Mean}_{\Phi(\theta)} \left\{ p(t^1; t^0_{\text{static}}, \hat{\Omega}_M, \theta) \right\}} \tag{3.17}$$

$$\mathcal{T}_{\text{static}} = \left\{ t^1 \in \mathbb{R} \mid \min_{u \in \Phi(\theta)} f(t^1; t^0_{\text{static}}) > \lambda \ \forall \ \theta \right\} \tag{3.18}$$

This optimization favors a beam profile wide enough to encompass the entire object at every view in the miscentered case. This approach is consistent with the traditional engineering design choice in which a larger (i.e., less "aggressive") bowtie filter is conservatively selected to maintain image quality for an object with both width variability and miscentering.

3.2.5 Image Reconstruction

FDK reconstructions were performed with a Hann window, 0.8 Nyquist frequency cutoff, 512 x 512 x 220 voxel image volume and a 0.5 mm isotropic voxel size. For bowtie filter studies, a simple additional gain scan associated with the bowtie at each position in the filter trajectory is necessary. However, as was discussed extensively in Chapter 2, the MADs are susceptible to focal

spot changes as well as spectral effects that may introduce artifacts in the reconstruction, necessitating a modified reconstruction pipeline (Figure 2.9).

For MAD reconstructions, the mean measurements $\bar{y}$ at projection θ are modeled by

$$\bar{y}(\theta) = g_{I_0} g_D \left(g_M(\theta) e^{-\hat{\beta}(\theta)\mu l} + s(\theta) \right) \tag{3.19}$$

where g_{I_0} is the emitted x-ray distribution from the tube, g_D is the x-ray detector sensitivity, g_M is the blur corrected MAD transmissivity and $\hat{\beta}$ is the first-order spectral correction factor discussed in Chapter 2. This model differs from Equation 2.9 only in the addition of a constant (shift-invariant) x-ray scatter term s.

A method to estimate and subtract the scatter signal from the data was also employed. This is particularly important to eliminate the bias that occurs when imaging through the very low transmissivity regions of the bowtie and dual-MAD. For the CTDI phantom studies outlined in Section 3.2.4.2, $s(\theta)$ was estimated by comparing reprojections of a binarized image volume with ideal attenuation $\mu_{PMMA}(\bar{E})$ against the actual measurements at the center of the object to obtain a constant scatter correction (per projection angle). This same correction was applied for both dynamic and static cases for each of the three filters investigated for consistency. Though more sophisticated methods for scatter correction could be applied, such as Monte Carlo methods (Zhao et al., 2016; Sisniega et al., 2011), this method was chosen for its simplicity. No scatter correction was applied for the anthropomorphic head data.

3.3 Results

3.3.1 Filter Trajectories

3.3.1.1 Performance of Trajectory Metrics

The five candidate trajectory designs for each of the three beam filters are summarized in Figure 3.6 for an object with 4 cm of miscentering. Ordinarily, one might presume $\mathrm{Std}_{\Phi}\{\cdot\}$ – i.e., a spatial variance penalty (or equivalently, spatial standard deviation) on the interior object region – to be the most appropriate criteria for selecting $f(t)$, as this reflects the commonly used uniform signal design objective for bowtie filters in CT (Toth et al., 2005; Wunderlich and Noo, 2007). The intuitive advantage to computing the standard deviation penalty over the entire detector length U would be of increased importance for CT detectors with limited dynamic range. However, as observed in Figure 3.6a, all design objectives were approximately equivalent in the aluminum bowtie case. Because the bowtie was designed specifically for this object, there is little contribution to the spatial variance from the fluence outside the object, making the computation over $\mathrm{Y} = U$ or $\mathrm{Y} = \Phi$ almost identical. This result was also consistent with the intuition that the beam shape is approximately independent of filter translation and that the beam simply shifts with translation (Figure 3.3a), meaning the mean fluence penalty has little effect on the result. Hence, while there is no implicit consideration of the beam shape $f(t)$ in the CM approach, the simplest objective appears to work well in the case where the filter is perfectly matched to the object and was therefore chosen for the bowtie image quality studies.

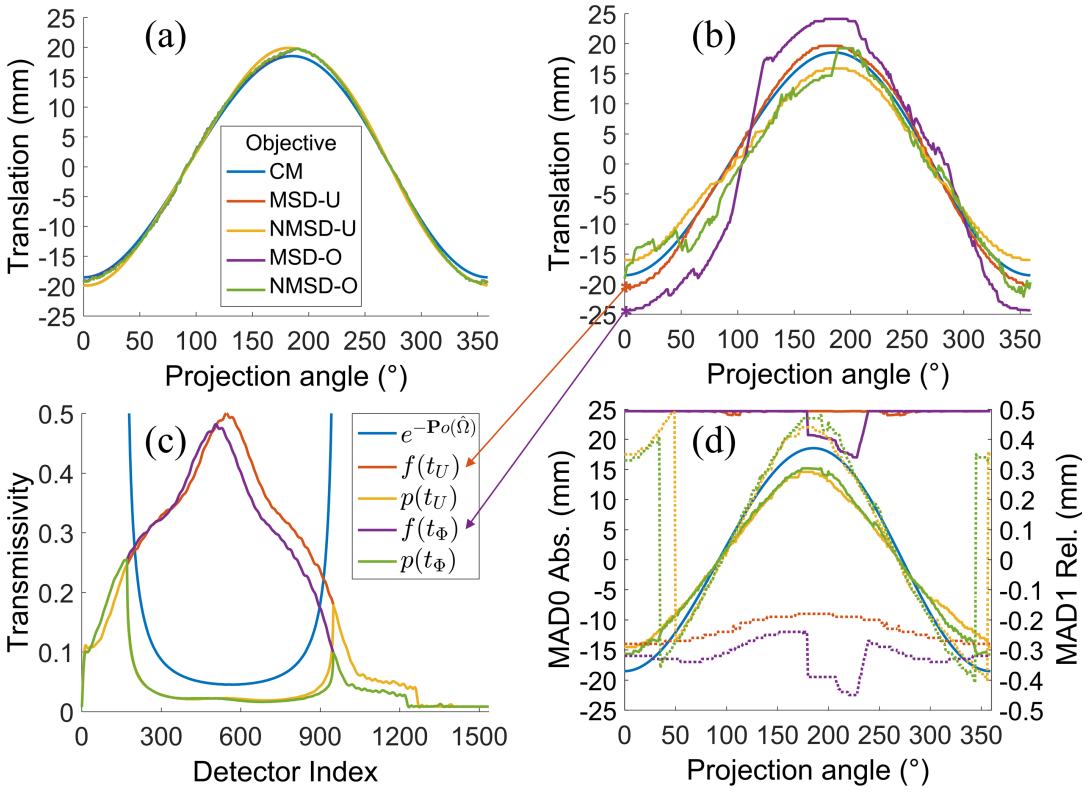

Figure 3.6: Optimizers considered for (a) the bowtie, (b) single-MAD, and (d) dual-MAD trajectories with the shared legend shown in (a). (c) Illustration of the differences between the $\text{Std}_U\{p\}$ and $\text{Std}_\Phi\{p\}$ objectives in the single-MAD case for the t_U and t_Φ positions respectively (marked by *) at $\theta = 0°$. (d) plots the relative MAD1 translations (dotted lines) overlaid on the absolute MAD0 positions (solid lines). The CM approach, in blue, provides a reference for the location of the projected object center but does not represent its own 2DOF trajectory in (d). All plots (a - d) were computed for the CTDI phantom with offset $e_{\text{ap}} = -4.02$ cm.

For the single-MAD filter, there was more variability between the objectives, as seen in Figure 3.6b. We see that the MSD approach is able to accommodate trade-offs in beam centering and beam width not present in the traditional bowtie (Figure 3.3b). That is, the single-MAD beam width is narrower for off-center translations, and the MSD objective can accommodate these variations by increasing the amplitude of the trajectory slightly relative to the CM approach. More significantly, we observe that the MSD-O metric resulted in a trajectory that was significantly different from the others. With a

symmetric, perfectly designed fluence profile (e.g., the aluminum bowtie case), the only way to minimize the spatial standard deviation of the detector fluence is to center the beam on the object. For symmetric fluence profiles that cannot flatten the detector fluence and/or are not matched in width to the object (e.g., the single MAD for the CTDI phantom), it was possible to find a solution that will further lower Std_Φ with an asymmetric profile. As shown in Figure 3.6c, $\text{Std}_\Phi\{p(t_U)\}$ and $\text{Std}_\Phi\{p(t_\Phi)\}$ were 0.0244 and 0.0228 respectively, but $f(t_U)$ was more centered on the object than $f(t_\Phi)$, reflected by the fact that $\text{Std}_U\{p(t_U)\}$ and $\text{Std}_U\{p(t_\Phi)\}$ were 0.0497 and 0.0530, respectively. We note that the largest contributors to the MSD-U metric were the two large peaks just outside of Φ. While both solutions gave similar uniformity within Φ, the penalty computed over $\text{Y} = U$ added an implicit penalty for asymmetry by comparing the fluence on either side of the object region, therefore tending to favor more "equalization" of the two peaks. For this reason, the MSD-U objective was chosen for the image quality studies for its ability to encourage improved centering of the beam on the object, which would tend to replicate the noise distribution of the centered case and promote more consistent imaging performance. While the NMSD metrics yielded similar results to MSD-U, the mean fluence penalty yielded minimal advantage in the single-MAD case because of the lack of beam width flexibility, and would unfairly penalize the beam narrowing due to obliquity at large displacements, preventing a full amplitude trajectory.

As seen in Figure 3.6d, the MSD objectives failed for the dual-MAD filter because the second degree of translational freedom allowed solutions that

minimize spatial standard deviation by simply pushing the overall fluence to zero. To avoid these trivial solutions and accommodate both beam centering and width considerations, the NMSD-O design objective was chosen, where utilizing the support region $\Phi(\theta)$ is preferred for optimal dose utilization within the object. Though it seems that the MAD0 position could be set heuristically using the CM approach, there would be ambiguity in computing the appropriate MAD1 translation, and such a design strategy would not work in general for other types of dynamic filters (e.g., a piecewise linear attenuator (Hsieh et al., 2016)).

Table 3.1 summarizes the pairings of beam filtration methods and selected trajectory design strategies ($\hat{t}_b$, $\hat{t}_s$, and $\hat{t}_d$ for the bowtie, single MAD and dual MAD, respectively).

Table 3.1: Summary of Selected Trajectory Designs

Beam Filter	Design Strategy	Design Objective
Bowtie	CM	$\hat{t}_b(\theta) = SFD\frac{r\cos(\theta-\phi)}{SAD+r\sin(\theta-\phi)}$
Single MAD	MSD-U	$\hat{t}_s(\theta) = \arg\min_{t\in\mathcal{T}_1(\theta)} \mathrm{Std}_U\{p(t;\theta)\}$
Dual MAD	NMSD-O	$\hat{t}_d(\theta) = \arg\min_{t\in\mathcal{T}_2(\theta)} \frac{\mathrm{Std}_{\Phi(\theta)}\{p(t;\theta)\}}{\mathrm{Mean}_{\Phi(\theta)}\{p(t;\theta)\}}$

3.3.1.2 Estimated Filter Trajectories for Image Quality Studies

The calculated filter trajectories for the three beam filtration strategies and the miscentered 16 cm CTDI phantom are summarized in Figure 3.7. Consistent with intuition, these trajectories were largely sinusoidal with an amplitude equal to approximately half of the miscentering offset, which was

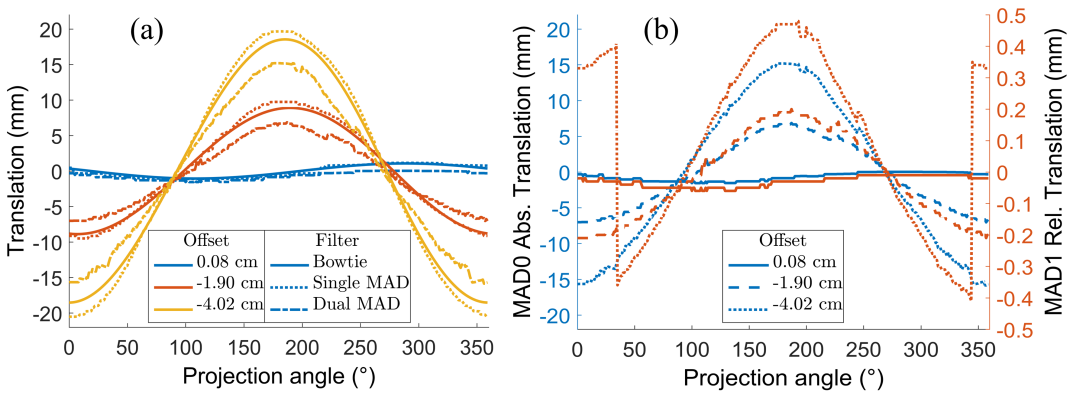

Figure 3.7: (a) Estimated filter trajectories for each filter and miscentering scenario, where the "offset" was the estimated e_{ap}. (b) Dual MAD trajectories for the same miscentering offsets as (a).

consistent with our CT system geometry where the magnification of the filter, $SAD/SFD \approx 2$. For the MAD filters, the trajectories were sinusoidal but not as smooth, which may be attributable to non-smooth transitions between the measured MAD modulation patterns. In the single-MAD case, the MSD-U approach yielded a slightly larger amplitude than the CM approach for the bowtie because, for a (left) miscentered object and fan-beam projection, the projection center-of-mass is skewed to the left of the projected objected center. This object obliquity effect becomes more pronounced for larger miscentering offsets, as is evident in Figure 3.7a. The MSD-U metric is able to accommodate this effect and compensate for the beam narrowing observed with the single-MAD beam patterns. For this same reason, a slight left-ward phase shift was observed in the MSD-U trajectory where the filter begins to shift farther than in the CM approach to account for this obliquity.

The dual-MAD trajectory was similar to that of the single MAD except with an amplitude of translation smaller than even that of the bowtie. As seen from Figure 3.3c, the general decrease in beam amplitude as a function

of displacement means that there was additional cost for large MAD0 shifts according to the NMSD metric, which penalizes lower mean fluence levels. Additionally, the calibration showed that there is a small phase shift in the profiles achievable within one period of relative MAD1 translation as a function of absolute MAD0 position. As seen in Figure 3.7b, the relative MAD1 translation followed the same general trend as MAD0, indicating that approximately the same beam width was selected at every MAD0 position. For 4 cm of miscentering, the relative position of MAD1 experiences "phase-wrapping" where a sharp transition from -0.4 to $+0.4$ mm was observed due to the fact that the MAD1 calibration was only conducted within a single period. Despite this apparent discontinuity, the absolute translation profile of MAD1 was still relatively smooth and hence did not cause practical difficulties for our actuation system. While it appears this "phase-wrapping" might have been avoided by extending the calibration, the neighboring period of patterns are not identical due to MAD obliquity effects, so the NMSD objective may still have chosen the profile closest to the center, which has the highest amplitude.

3.3.2 Dose and Image Noise Measurements

Figures 3.8, 3.9 and 3.10 summarize the results of the CTDI phantom studies. For the static aluminum bowtie, miscentering had a large effect on both dose and image noise: for 4 cm of offset (toward the left of the detector), location 3 saw a 39% dose increase and a 22% noise decrease while location 5 saw a 42% dose decrease and a 173% noise increase relative to the centered condition (Figures 3.9a and 3.10a). This large noise increase at location 5 and

the general noise increase at all other locations other than 3 were the result of imaging through the edge of the bowtie, where the transmissivity decreased sharply down to approximately 4%. Moving from 2 to 4 cm of miscentering, projections of the dosimeter locations fell in this low transmissivity region for some portion of the 360° acquisition. Because of the "aggressive" design of this bowtie to perfectly flatten the detector fluence for the 16 cm CTDI phantom and the smaller size of this object, the quantitative results observed here differ significantly from those of previous studies. The study by Toth, Ge, and Daly (2007), for example, employed bowties that taper more moderately to a minimum transmissivity of 10%, while Habibzadeh et al. (2010) also utilized GE Healthcare's "large-body" bowtie for their study. We note here that the dose measurements shown do not perfectly reflect the inverse square root proportionality with the noise measurement because of the scatter correction that is applied before image reconstruction.

With the dynamic bowtie the variations were largely mitigated, with the dose and noise remaining close to baseline levels for all dosimeter locations as well as the overall $CTDI_w$, as seen in Figures 3.9b and 3.10b. Figures 3.8a-3.8c show that use of the dynamic filter promoted homogeneous noise in the reconstruction whereas the static filter caused a significant noise increase on the left and decrease on the right side of the object. A slight asymmetry from left to right in the noise distribution was observed in the case of 4 cm miscentering, but this may have been intrinsic to the fact that the 1DOF filter has a fixed beam shape. That is, the fixed beam shape cannot account for the combination of obliquity and depth-dependent magnification effects that

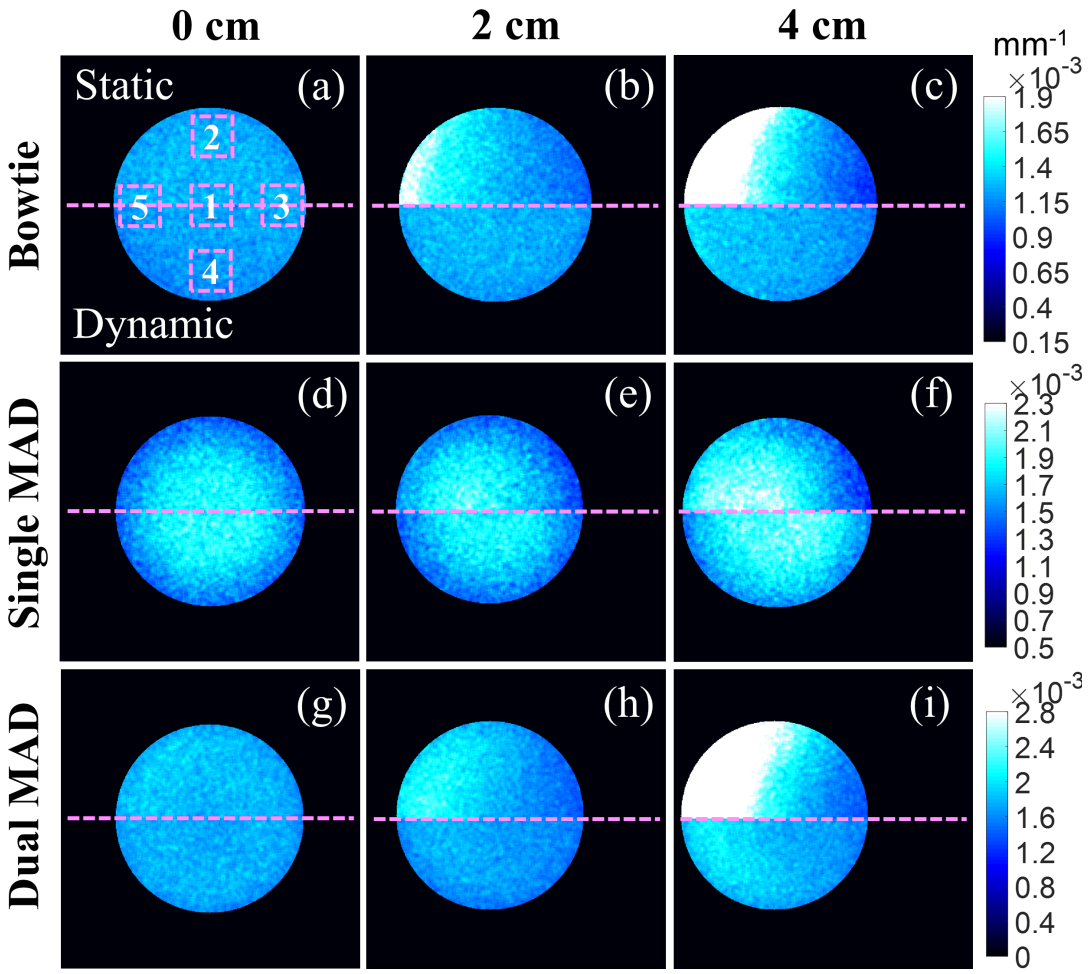

Figure 3.8: Noise maps for each scenario showing the static/dynamic cases split into the top/bottom halves (exploiting symmetry for visualization) masked by $o(\hat{\Omega})$ to show only the object region. The window was adjusted to reflect the distinct noise levels for each filter case. ROIs used to quantify noise in Figures 3.9 and 3.10 are labeled in the top-left (not to scale) and match the numbering shown in Figure 3.5a.

occur with the miscentered object, and so even the translating bowtie cannot perfectly flatten the fluence for the miscentered object.

The static single-MAD data shows similar left-to-right dose and noise gradients as those observed with the aluminum bowtie. Because the low transmissivity region only approached 10%, however, the noise penalty for location 5 at 4 cm offset was not as severe as with the bowtie, only reaching

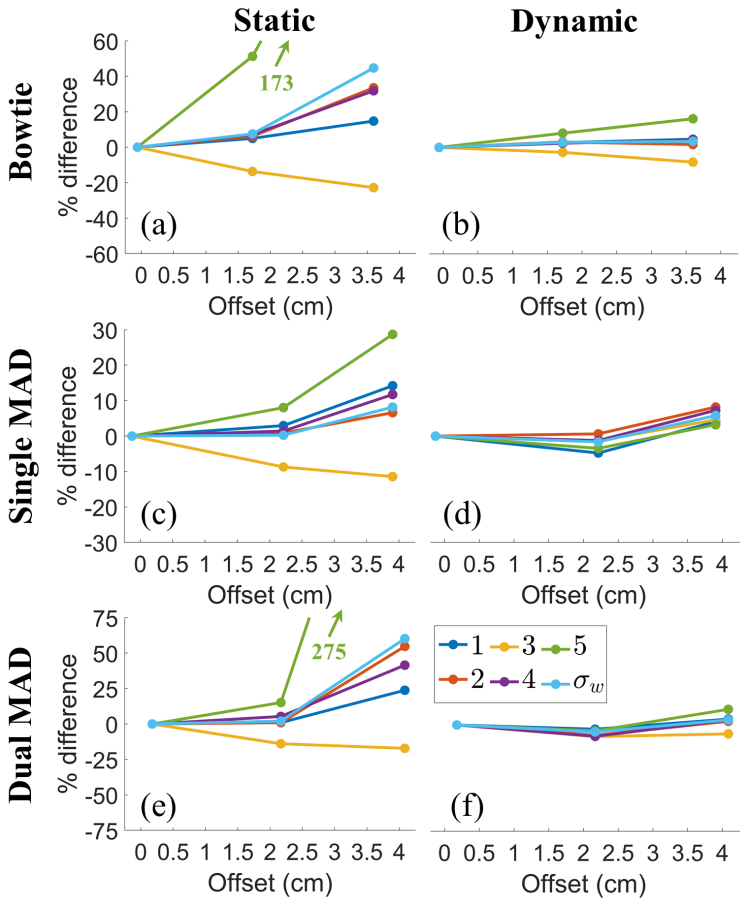

Figure 3.9: Quantitative noise results for the static/dynamic aluminum bowtie, single-MAD, and dual-MAD filters. The noise at each dosimeter location (locations 1-5) was plotted as a function of the amount of estimated linear miscentering e_{ap}. Note that the x-axis has been inverted so that increased miscentering follows from left to right.

29% as seen in Figure 3.9c. The noise levels as observed in Figure 3.8d were higher overall, which is attributed to the overall lower fluence levels of the MAD (55% vs 90% maximum transmissivity as shown in Figure 3.3e). The irregular single-MAD fluence profiles were also suboptimal for promoting uniform detector fluence for the 16 cm CTDI phantom, leading to a bowl-shaped noise distribution with higher observed central noise in Figure 3.8d. Additional narrowing and decreasing fluence levels for large shifts (9% lower maximum transmissivity for a 2 cm shift corresponding to 4 cm offset as

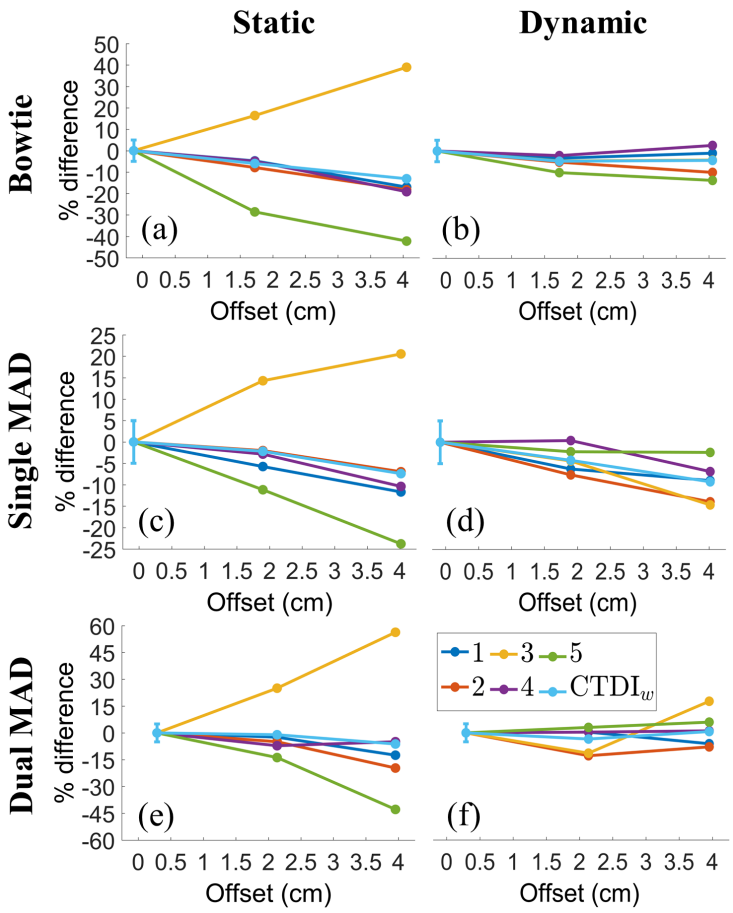

Figure 3.10: Quantitative dose results for the static/dynamic aluminum bowtie, single-MAD, and dual-MAD filters. Error bars on the centered condition indicate the inherent 5% uncertainty in dose measurements made at ambient conditions, according to the ion chamber manufacturer ((*Radiation Measurement Systems User Guide* 2013)).

seen in Figure 3.3b) lead to overall dose decreases for all locations at 4 cm miscentering and overall higher noise (Figures 3.9d, 3.10d and 3.8f), even with the dynamic single MAD. Despite these differences, Figure 3.8 demonstrates that the dynamic MAD was still able to distribute noise similarly to the baseline while the static filter could not. Notably, Figure 3.9d shows that there was less left-to-right variation in this case than for the bowtie, which may be related to the broad fluence profiles of the single MAD, which can help mitigate the inability to modulate beam width.

The trends observed for the dual-MAD case were, in general, very similar to those of the bowtie. The overall observed noise levels for the centered case shown in Figure 3.8g were 1.9×10^{-3} mm^{-1} for the dual MAD compared to 1.2×10^{-3} mm^{-1} for the bowtie, representing approximately a 50% increase that intuitively reflects the noise proportionality $\sigma \propto \frac{1}{\sqrt{\text{Dose}}}$ where the dual-MAD fluence levels were at 40% (maximum transmissivity) compared to 90% for the bowtie (as shown in Figure 3.3e). Because of the transmissivity constraint applied within Φ, the static beam profile was wider than that of the bowtie and hence the noise increase in the 2 cm miscentering case was not as severe. However, due to the more "aggressive" design of the dual MAD, a more dramatic noise penalty was observed at location 5 for 4 cm of miscentering with a static filter (Figure 3.9e). With the dynamic dual MAD, dose and image noise distribution were more homogeneous and similar to the baseline. More left-to-right variation in the observed noise distribution was apparent for the 4 cm case (Figure 3.8i) than the bowtie, though still within 10% of the baseline as seen in Figure 3.9f. This asymmetry is believed to be due to the smaller amplitude of the filter trajectory resulting from the tradeoff between fluence uniformity and mean fluence in the NMSD metric, which has the effect of slightly overexposing the right part of the object and underexposing the left. Though it was not applied for this study, techniques such as tube-current modulation could be used to help eliminate the residual non-uniformities in both the bowtie and dual-MAD cases.

The peak noise measurements for each combination of miscentering and beam filter along with the associated noise-adjusted exposure calculations

Table 3.2: Dose reduction with dynamic filtration.

	Peak Noise			Noise-adjusted Dose		
Beam Filter	0 cm	2 cm	4 cm	0 cm	2 cm	4 cm
Bowtie – Static	100%	149%	297%	100%	223%	881%
Bowtie – Dynamic	100%	99.7%	104%	100%	99.4%	109%
Single MAD – Static	100%	107%	116%	100%	115%	135%
Single MAD – Dynamic	100%	96.2%	104%	100%	92.5%	109%
Dual MAD – Static	100%	117%	423%	100%	138%	1790%
Dual MAD – Dynamic	100%	97.4%	114%	100%	94.9%	129%

are shown in Table 3.2. The values were normalized to the centered case in each row. In general, the dynamic filter would require significantly less dose adjustment in order to maintain the same image quality for a miscentered object. For the “aggressive" beam filters, an 8-fold and 13-fold decrease in noise-adjusted dose is achievable with the dynamic bowtie and dual-MAD filters, respectively. For the more moderate single-MAD filter, 24% dose savings are possible for the dynamic vs the static filter to maintain the same peak variance at 4 cm of miscentering, which agrees with estimates of the noise-adjusted dose increase from previous studies using less aggressive bowties (Toth, Ge, and Daly, 2007).

3.3.3 Dynamic Dual-MAD Filtration for the Anthropomorphic Head Phantom

Application of dynamic beam modulation to the anthropomorphic head phantom using the dual-MAD filter is illustrated in Figures 3.11 and 3.12. The calibrated object models in Figures 3.11a and 3.11c reasonably approximate

the shape and location of the real object in the FOV. According to the calibration, e_{ap} and e_{lat} were -0.20 cm and 0.14 cm, respectively, for the centered case and -2.29 cm and 1.71 cm, respectively, for the miscentered case. Because of the linear miscentering in both x and y directions, the anthropomorphic head had inherent width variability, projection-dependent obliquity and centering effects that required accommodation by the dynamic filtration strategy. The dynamic filter trajectory for the miscentered case in Figure 3.11d shows that the (relative) MAD1 trajectory had a much larger amplitude, reflecting the need for dynamic width control for an elliptical object. The relative position of MAD1 for the static trajectory indicates the selection of a wide beam profile by inspection of Figure 3.3d.

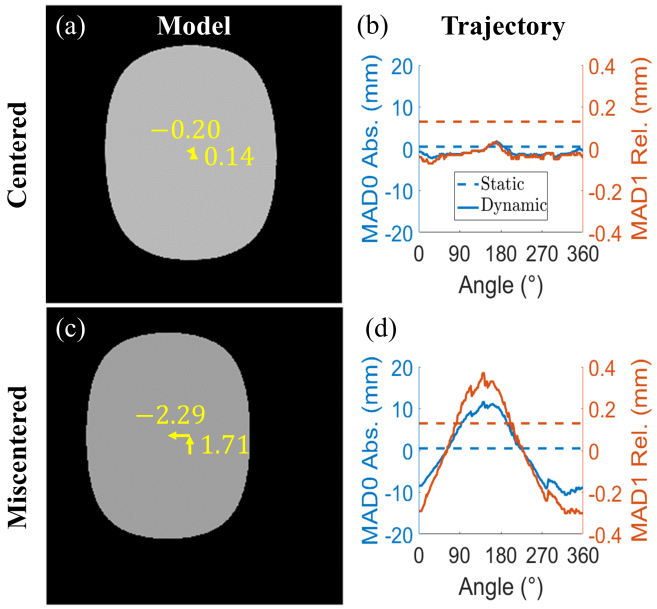

Figure 3.11: Calibrated object models (a and c) and calculated dual-MAD motion trajectories (b and d) for the head phantom study with a centered and miscentered object.

The reconstructed images demonstrate the lack of ring artifacts arising from the MAD filter; however some beam hardening and cupping effects are

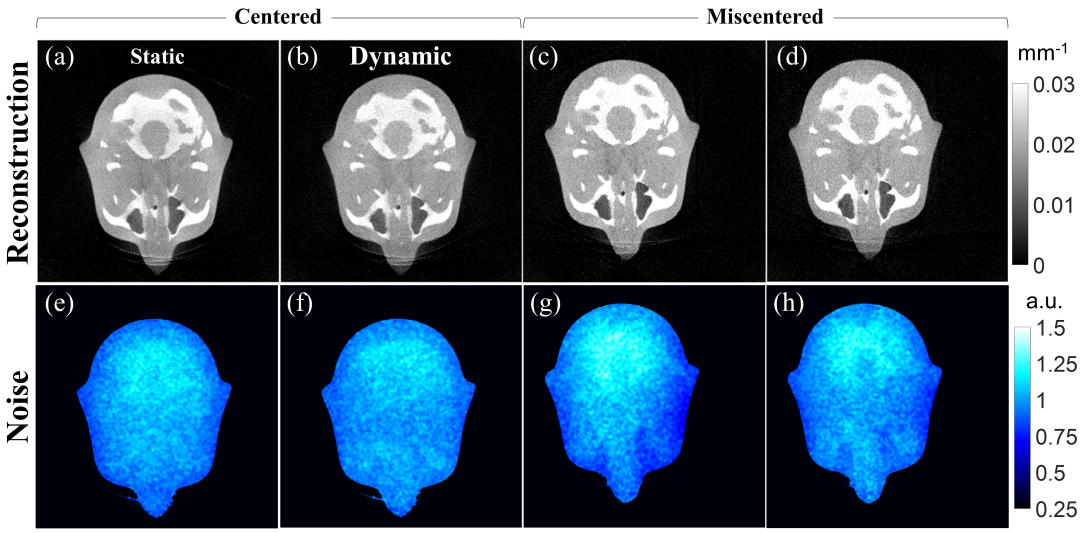

Figure 3.12: Results of the head phantom study comparing static and dynamic filter trajectories, with the reconstructed axial slices (a - d) and the associated noise maps (e - h) for both centered and miscentered cases. The yellow arrows indicate the direction and amount of miscentering in cm.

observed, as no scatter or beam hardening correction was applied. Some bias is evident at the bottom of the image in the nose region that was outside of the object model and hence well within the low transmissivity region of the filters (contributing to artifact sensitivity). From the noise maps, we see that the noise distribution was largely homogeneous in the centered case (Figures 3.12e and 3.12f) with some variations due to anatomical inhomogeneity and the lack of tube-current modulation. However, the differences between the static and dynamic filter are still apparent. Consistent with our expectation from the results observed in from Figure 3.8i, the dynamic filter was able to distribute noise similarly to baseline in the miscentered case (Figure 3.12h), whereas significant increases in image noise in the top left portion and significant decreases in the bottom right portion of the image are observed in the static miscentered case (Figure 3.12g), despite the use of a broad beam profile. A

slight noise gradient from top left to bottom right was still observed in the dynamic case, which may again be attributable to the same reasons described earlier in Section 3.3.2 for the 4 cm dual-MAD case.

3.4 Discussion

In this work, dynamic beam modulation for miscentered patients was demonstrated using three beam filtration strategies. For the bowtie, simple translation of the filter using a basic trajectory estimation approach based on centering the beam on the center of the patient was used. For the more complex beam modulators based on the dual-MAD filter, we considered a more sophisticated metric seeking an optimal trade-off between minimal variation in the detected signal and maximal mean detected fluence. In general, a simple monolithic filter can be actuated effectively using the simple CM design objective if well-matched to the object, while more complex dynamic filters require an objective that can balance field-flattening and overall signal levels like the NMSD-O metric. All three scenarios demonstrate the ability to keep the spatial distribution of dose and image noise at baseline levels (i.e., compared to static filtration with a centered object) across arbitrary levels of miscentering for the homogeneous CTDI object.

The results also strongly suggest that the dual MADs operate effectively as dynamic bowtie filters, and that their capability for beam width control allows for increased uniformity of image properties. In particular, the noise gradients observed in the static filtering scenarios with miscentered objects illustrate two key effects that need to be accommodated by a dynamic filter:

1) patient centering, and 2) depth-dependent magnification of projection data, which are compensated by beam centering control and beam width modulation, respectively. Moreover, variations in patient size and anatomical site result in additional variation in the width of patient projections. Thus, while all investigated methods demonstrate improved uniformity in dose and noise, fluence-field modulation strategies like the dual-MAD filter may have additional advantages across a greater range of clinical scenarios.

While the studies conducted here using dynamic beam modulation showed greater control of dose and noise properties, the methods did not use additional exposure control (e.g., tube current modulation) as a function of rotation angle (Gies et al., 1999). Automatic exposure control is another important element of dose reduction and noise minimization which can have a significant impact on noise correlations in reconstructed images. Ongoing studies are exploring the combination of spatial beam modulation in conjunction with angular beam modulation of the overall fluence for additional control and improvements in dose utilization. Similarly, while the studies presented here focused on a simple metric of image quality (i.e., noise in FBP reconstructions), more sophisticated image quality metrics tailored to specific clinical tasks may be more appropriate. Recent studies have suggested that such task-based optimization as well as advanced model-based reconstruction methods can lead to non-traditional modulation strategies (Gang, Siewerdsen, and Stayman, 2017b; Gang, Siewerdsen, and Stayman, 2017a). Future studies will include investigations of optimized beam modulation for miscentered patients using such task-based metrics and advanced reconstruction.

In conclusion, a workflow and methodology was developed to dynamically position beam filters during CT image acquisition. The techniques are generally applicable to other beam filtration strategies, and promote consistent imaging and dose performance for arbitrary patient positioning. Such advantages could ease patient setup requirements and reduce repeat scanning in cases of poor positioning. Such benefits are particularly applicable in challenging clinical settings like ER CT, where a simplified patient setup procedure will benefit workflow and maintain the dose advantages of spatial beam shaping.

References

Mao, Andrew, William Shyr, Grace J. Gang, and Joseph Webster Stayman (2018). "Dynamic beam filtering for miscentered patients". In: *Proc. of SPIE Medical Imaging 2018: Physics of Medical Imaging* 10573, 105730U1–7. DOI: 10.1117/12.2293696.

Mao, Andrew, Grace J. Gang, William Shyr, Reuven Levinson, Jeffrey H. Siewerdsen, Satomi Kawamoto, and Joseph Webster Stayman (2018 (submitted)). "Dynamic fluence field modulation for miscentered patients in computed tomography". In: *Journal of Medical Imaging*.

Toth, T L, E Cesmeli, A Ikhlef, and T Horiuchi (2005). "Image quality and dose optimization using novel x-ray source filters tailored to patient size". In: *Progress in Biomedical Optics and Imaging - Proceedings of SPIE* 5745.I, pp. 283–291. DOI: 10.1117/12.595465.

Wunderlich, Adam and Frédéric Noo (2007). "Achieving uniform noise in direct fan-beam CT reconstruction through bowtie filter design". In: *IEEE Nuclear Science Symposium Conference Record* 6, pp. 4379–4382. DOI: 10.1109/NSSMIC.2007.4437083.

Toth, T., Z. Ge, and M. P. Daly (2007). "The influence of patient centering on CT dose and image noise". In: *Medical Physics* 34, pp. 3093–3101. DOI: 10.1118/1.2748113.

Habibzadeh, M. A., M. R. Ay, A. R. Kamali Asl, H. Ghadiri, and H. Zaidi (2010). "The Influence of Patient Miscentering on Patient Dose and Image Noise in Two Commercial CT Scanners". In: *XII Mediterranean Conference on Medical and Biological Engineering and Computing 2010 IFMBE Proceedings*, 327âĂŞ–330. DOI: 10.1007/978-3-642-13039-7_82.

Szczykutowicz, Timothy P., Andrew DuPlissis, and Perry J. Pickhardt (2017). "Variation in CT number and image noise uniformity according to patient positioning in MDCT". In: *American Journal of Roentgenology* 208.5, pp. 1064–1072. DOI: 10.2214/AJR.16.17215.

Li, Jianhai, Unni K. Udayasankar, Thomas L. Toth, John Seamans, William C. Small, and Mannudeep K. Kalra (2007). "Automatic patient centering for MDCT: Effect on radiation dose". In: *American Journal of Roentgenology* 188.2, pp. 547–552. DOI: 10.2214/AJR.06.0370.

Li, Hong, Kaihua Liu, Hang Sun, Nan Bao, Xu Wang, Shi Tian, Shouliang Qi, and Yan Kang (2014). "Automatic heart positioning method in computed tomography scout images". In: *Bio-Medical Materials and Engineering* 24.6, pp. 3277–3286. DOI: 10.3233/BME-141150.

Mayo-Smith, William W., Amy K. Hara, Mahadevappa Mahesh, Dushyant V. Sahani, and William Pavlicek (2014). "How I Do It: Managing Radiation Dose in CT". In: *Radiology* 273.3, pp. 657–672. DOI: 10.1148/radiol.14132328.

Lambert, J. W., S. Kumar, J. S. Chen, Z. J. Wang, R. G. Gould, and B. M. Yeh (2015). "Investigating the CT localizer radiograph: Acquisition parameters, patient centering and their combined influence on radiation dose". In: *British Journal of Radiology* 88.1048, pp. 8–12. DOI: 10.1259/bjr.20140730.

Hara, Amy K., Clinton V. Wellnitz, Robert G. Paden, William Pavlicek, and Dushyant V. Sahani (2013). "Reducing body CT radiation dose: Beyond just changing the numbers". In: *American Journal of Roentgenology* 201.1, pp. 33–40. DOI: 10.2214/AJR.13.10556.

Guasti, M. Fernandez (1992). "Analytic geometry of some rectilinear figures". In: *Int. J. Math. Educ. Sci. Technol* 23 (6), pp. 895–901.

Siddon, R L (1984). "Fast calculation of the exact radiological path for a three-dimensional CT array." In: *Medical Physics* 12.2, pp. 252–255. DOI: 10.1118/1.595715.

Nelder, J. A. and R. Mead (1965). "A Simplex Method for Function Minimization". In: *The Computer Journal* 7.4, 308âĂŞ313. DOI: 10.1093/comjnl/7.4.308.

Punnoose, J., J. Xu, A. Sisniega, W. Zbijewski, and J. H. Siewerdsen (2016). "Technical Note: Spektr 3.0 - A computational tool for x-ray spectrum modeling and analysis". In: *Medical Physics* 43.8, pp. 4711–4717. DOI: 10.1118/1.4955438.

Kak, Avinash C. and Malcolm Slaney (2001). *Principles of Computerized Tomographic Imaging*. Philadelphia, PA, USA: Society for Industrial and Applied Mathematics. ISBN: 0-89871-494-X.

Mail, N., D. J. Moseley, J. H. Siewerdsen, and D. A. Jaffray (2008). "The influence of bowtie filtration on cone-beam CT image quality". In: *Medical Physics* 36.1, pp. 22–32. DOI: 10.1118/1.3017470.

Xu, Jennifer, Alejandro Sisniega, Wojciech Zbijewski, Hao Dang, J. Webster Stayman, Xiaohui Wang, David H. Foos, Nafi Aygun, Vassillis E. Koliatsos, and Jeffrey H. Siewerdsen (2016). "Evaluation of detector readout gain mode and bowtie filters for cone-beam CT imaging of the head". In: *Physics in Medicine and Biology* 61.16, pp. 5973–5992. DOI: 10.1088/0031-9155/61/16/5973.

Stayman, J. Webster, Aswin Mathews, Wojciech Zbijewski, Grace Gang, Jeffrey Siewerdsen, Satomi Kawamoto, Ira Blevis, and Reuven Levinson (2016). "Fluence-Field Modulated X-ray CT using Multiple Aperture Devices". In: *Proc. of SPIE Medical Imaging 2016: Physics of Medical Imaging* 9783, pp. 97830X1–6. DOI: 10.1117/12.2214358.

Mathews, A. J., S. Tilley, G. Gang, S. Kawamato, W. Zbijewski, J. H. Siewerdsen, R. Levinson, and J. W. Stayman (2016). "Design of dual multiple aperture devices for dynamical fluence field modulated CT". In: *Conf Proc Int Conf Image Form Xray Comput Tomogr* 4, pp. 29–32.

Feldkamp, L A, L C Davis, and J W Kress (1984). "Practical cone-beam algorithm". In: *J. Opt. Soc. Am. A* 1.6, pp. 612–619. DOI: 10.1364/JOSAA.1.000612.

Hsieh, Scott S. and Norbert Joseph Pelc (2014). "Algorithms for optimizing CT fluence control". In: *Proceedings of SPIE* 9033, pp. 90330M1–6. DOI: 10.1117/12.2042542.

Hsieh, Scott S., Dominik Fleischmann, and Norbert J. Pelc (2014). "Dose reduction using a dynamic, piecewise-linear attenuator". In: *Medical Physics* 41.2, p. 021910. DOI: 10.1118/1.4862079.

Otsu, Nobuyuki (1979). "A Threshold Selection Method from Gray-Level Histograms". In: *IEEE Transactions on Systems, Man, and Cybernetics* 9.1, pp. 62–66. DOI: 10.1109/TSMC.1979.4310076.

Zhao, Wei, Don Vernekohl, Jun Zhu, Luyao Wang, and Lei Xing (2016). "A model-based scatter artifacts correction for cone beam CT". In: *Medical Physics* 43.4, pp. 1736–1753. DOI: 10.1118/1.4943796.

Sisniega, A., M. Abella, E. Lage, M. Desco, and J. J. Vaquero (2011). "Automatic Monte-Carlo based scatter correction for X-ray cone-beam CT using general purpose graphic processing units (GP-GPU): A feasibility study". In: *IEEE Nuclear Science Symposium Conference Record*, pp. 3705–3709. DOI: 10.1109/NSSMIC.2011.6153699.

Hsieh, Scott S, Mark V Peng, Christopher A May, Picha Shunhavanich, Dominik Fleischmann, and Norbert J Pelc (2016). "A prototype piecewise-linear dynamic attenuator". In: *Physics in Medicine and Biology* 61.13, pp. 4974–4988. DOI: 10.1088/0031-9155/61/13/4974.

Radiation Measurement Systems User Guide (2013). Radcal Corporation.

Gies, Michael, Willi A. Kalender, Heiko Wolf, Christoph Suess, and Mark T. Madsen (1999). "Dose reduction in CT by anatomically adapted tube current modulation. I. Simulation studies". In: *Medical Physics* 26.11, pp. 2235–2247. DOI: 10.1118/1.598779.

Gang, Grace Jianan, J H Siewerdsen, and J W Stayman (2017b). "Task-driven optimization of CT tube current modulation and regularization in model-based iterative reconstruction". In: *Physics in Medicine and Biology* 62.12, pp. 4777–4797. DOI: 10.1088/1361-6560/aa6a97.

Gang, G J, J H Siewerdsen, and J W Stayman (2017a). "Task-Driven Optimization of Fluence Field Regularization for Model-Based Iterative Reconstruction in Computed Tomography". In: *IEEE Transactions on Medical Imaging* 36.12, pp. 2424–2435.

Chapter 4

Summary and Conclusions

4.1 Summary of Key Developments and Findings

This dissertation presented methods for MAD-based FFM with regards to patient miscentering and developed a supporting correction pipeline for MAD imaging. This work pursued the following thesis:

Dynamic fluence-field modulation based on multiple aperture devices can be used to reconstruct diagnostic quality CT images, optimize dose utilization and improve uniformity of image properties in challenging clinical scenarios such as patient miscentering.

Key developments and findings in this dissertation are summarized in the following sections.

4.1.1 Preliminary MAD Correction Pipeline

Chapter 2 described the development of a pipeline to generate ring artifact-free reconstructions in MAD-based FFM. Corrections were devised to eliminate MAD bar patterns in projections of a uniform elliptical phantom, which

required a) consideration of focal spot changes (blooming and/or shifting) resulting in a mismatch between acquired and calibration MAD scans; and b) spectral effects resulting from x-ray penetration effects through the tungsten slits of the MAD. Blur correction was performed frame-to-frame using fiducials in the projection data, and spectral correction was calibrated using prior scans of variable thickness PMMA slabs. Blur correction was found to be most effective by modeling focal spot effects in a shift-variant manner, and spectral correction was found to perform best by optimizing a data-dependent scaling term for the first-order spectral coefficient estimated from the PMMA scans. Reconstructed images using the full MAD correction model demonstrated significantly reduced ring artifacts.

4.1.2 MAD-based FFM for Patient Miscentering

Chapter 3 presented methods to design dynamic FFM for the problem of patient miscentering in CT. Several possible design objectives for the filter trajectories were considered and analyzed in detail for three filters: a traditional bowtie, a single-MAD device, and dual-MAD filter. Proper selection of the trajectory design metric was found to be filter-dependent, but the results of physical experiments with all three filters demonstrated improved consistency in image performance and significant dose reduction possibilities in comparison to the static (non-moving) filter. The dual MAD was found to be particularly advantageous for accommodating the two key effects observed with patient miscentering, namely projection centering and depth-dependent magnification.

4.2 Future Directions

The correction pipeline described in Chapter 2 relies on fitting based on an air region in half of the MAD. However, integration into a commercial CT scanner would require a focal spot model that can be performed anywhere on the detector (likely at the lateral extent). This being said, focal spot control on clinical CT scanners is generally much more precise than in the fluoro x-ray tube used on the testbench scanner. If this is true, this may obviate the need for a sophisticated shift-variant blur model that was necessary to eliminate MAD artifacts on the testbench, and perhaps a shift-invariant blur estimation would suffice. Regardless, blur modeling is likely to be an essential tool for clinical implementation of the MAD system.

There are several avenues of future research to properly assess and validate the clinical utility of the MAD-based FFM approach. A comprehensive observer study using MADs should be pursued to assess whether the MAD filtering concept can offer significant diagnostic advantages to radiologists. Such a study would seek to incorporate MAD-based FFM into task-based acquisitions and use task-based image quality metrics to conduct clinical performance assessment using human observer models, as in Gang, Siewerdsen, and Stayman (2017b) and Gang, Siewerdsen, and Stayman (2017a). A rigorous analysis of the dose reduction possibilities for a wide range of clinical CT imaging scenarios using MAD-based FFM would offer concrete, tangible evidence for the advantages of MAD-based filtering. Finally, additional directions to explore include MAD-based VOI imaging (Wang et al., 2018 (accepted)) or physical realization of limited angle CT reconstruction, which

may offer further opportunities for dose reduction.

References

Gang, Grace Jianan, J H Siewerdsen, and J W Stayman (2017b). "Task-driven optimization of CT tube current modulation and regularization in model-based iterative reconstruction". In: *Physics in Medicine and Biology* 62.12, pp. 4777–4797. DOI: 10.1088/1361-6560/aa6a97.

Gang, G J, J H Siewerdsen, and J W Stayman (2017a). "Task-Driven Optimization of Fluence Field Regularization for Model-Based Iterative Reconstruction in Computed Tomography". In: *IEEE Transactions on Medical Imaging* 36.12, pp. 2424–2435.

Wang, Wenying, Grace J. Gang, Andrew Mao, Alejandro Sisniega, Jeffrey H. Siewerdsen, and J. Webster Stayman (2018 (accepted)). "Volume-of-interest CT Imaging with Dynamic Beam Filtering Using Multiple Aperture Devices". In: *The Fifth International Conference on Image Formation in X-ray Computed Tomography, Salt Lake City, UT, USA*.

Andrew W. Mao

3900 N. Charles St, Apt 1211
Baltimore, MD, USA 21218
+1 (513) 667-4384
andrewwmao@gmail.com
linkedin.com/in/andrewwmao

Education

Jan. 2017 – May 2018 **M.S.E. Biomedical Engineering**, *Johns Hopkins University*, Baltimore, MD, USA.
Concentration in Medical Imaging, Thesis Track

Aug. 2013 – Dec. 2016 **B.S. Biomedical Engineering**, *Johns Hopkins University*, Baltimore, MD, USA.
Concentration in Sensors & Instrumentation

Research Experience

Jan. 2017 – May 2018 **Graduate Research Assistant, Advanced Imaging Algorithms & Instrumentation Lab**, *Department of Biomedical Engineering, Johns Hopkins University*, Baltimore, MD, under J. Webster Stayman, Ph.D.

June 2016 – Aug. 2016 **Cardiology R&D Intern, Ultrasound Imaging & Interventions**, *Philips Research North America*, Cambridge, MA, under Torre Bydlon, Ph.D.

May 2015 – July 2015 **Undergraduate Research Intern, Evolution Innovation Laboratory**, *Department of Biomedical Engineering, National University of Singapore*, Singapore, Singapore, under Raye Chen-Hua Yeow, Ph.D.

Publications, Conference Proceedings, and Presentations

1. **Mao, A.**, Gang, G. J., Shyr, W., Levinson, R., Siewerdsen, J. H., Kawamoto, S. and Stayman, J. W., "Dynamic fluence field modulation for miscentered patients in computed tomography," Journal of Medical Imaging (2018), *submitted*.
2. **Mao, A.**, Shyr, W., Gang, G. J. and Stayman, J. W., "Dynamic beam filtering for miscentered patients," *Proc. of SPIE Medical Imaging 2018: Physics of Medical Imaging* 10573, 105730U1–7 (2018).
3. **Mao, A.**, Shyr, W., Gang, G. J. and Stayman, J. W., "Dynamic beam filtering for miscentered patients," at SPIE Medical Imaging, February 2018, Houston, TX, USA (oral presentation).
4. Gang, G. J., **Mao, A.**, Siewerdsen, J. H. and Stayman, J. W., "Implementation and Assessment of Dynamic Fluence Field Modulation with Multiple Aperture Devices," *The Fifth International Conference on Image Formation in X-ray Computed Tomography, Salt Lake City, UT, USA*, (2018), *accepted*.
5. Gang, G. J., **Mao, A.**, Wang, W., Siewerdsen, J. H., Mathews, A., Levinson, R. and Stayman, J. W., "Dynamic Fluence Field Modulation with Multiple Aperture Devices: Design, Implementation, and Assessment," *The 60th Annual Meeting of the AAPM, Nashville, TN, USA*, (2018), *accepted*.
6. Wang, W., Gang, G. J., **Mao, A.**, Sisniega, A., Siewerdsen, J.H. and Stayman, J. W., "Volume-of-interest CT Imaging with Dynamic Beam Filtering Using Multiple Aperture Devices," *The Fifth International Conference on Image Formation in X-ray Computed Tomography, Salt Lake City, UT, USA*, (2018), *accepted*.
7. Gang, G. J., **Mao, A**, Wang, W., Siewerdsen, J.H., Kawamoto, S., Levinson, R. and Stayman, J. W., "Dynamic fluence field modulation in CT with multiple aperture devices," *The 104th Annual Meeting of the RSNA, Chicago, IL, USA*, (2018), *submitted*.
8. Yap, H. K.*, **Mao, A.***, Goh, J. C. H. and Yeow, C., "Design of a Wearable FMG Sensing System for User Intent Detection During Hand Rehabilitation with a Soft Robotic Glove," *Proc. of the IEEE RAS and EMBS International Conference on Biomedical Robotics and Biomechatronics* 6, 781–786 (2016).

* *denotes equal authorship.*

Work and Service

Sep. 2013 – May 2017 **Co-President**, *Community School Initiative, Center for Social Concern, Johns Hopkins University*, Baltimore, MD.

Aug. 2014 – May 2017 **Head PILOT Learning Leader**, *Academic Advising, Johns Hopkins University*, Baltimore, MD.

Feb. 2017 – May 2017 **Grading Assistant, Systems Bioengineering II (580.422/722)**, *Department of Biomedical Engineering, Johns Hopkins University*, Baltimore, MD.

Jan. 2015 – May 2015 **Course Assistant, Intermediate Programming (600.120)**, *Department of Computer Science, Johns Hopkins University*, Baltimore, MD.

Honors and Awards

Robert F. Wagner All-Conference Student Paper Award, SPIE Medical Imaging 2018
Physics of Medical Imaging Student Paper Award, SPIE Medical Imaging 2018
Richard J. Johns Achievement Award 2017
Medtech Poster Award, JHU CBID Design Day 2016
Alpha Eta Mu Beta Biomedical Engineering Honor Society 2016
Tau Beta Pi National Engineering Honor Society 2015
Finalist, Qualcomm Tricorder X-Prize Competition 2014